

Air Force Institute of Technology

**AFIT Scholar**

---

Theses and Dissertations

Student Graduate Works

---

3-13-2007

## Point Spread Function Characterization of a Radially Displaced Scatterer Using Circular Synthetic Aperture Radar

Uttam K. Majumder

Follow this and additional works at: <https://scholar.afit.edu/etd>



Part of the [Signal Processing Commons](#)

---

### Recommended Citation

Majumder, Uttam K., "Point Spread Function Characterization of a Radially Displaced Scatterer Using Circular Synthetic Aperture Radar" (2007). *Theses and Dissertations*. 3146.  
<https://scholar.afit.edu/etd/3146>

This Thesis is brought to you for free and open access by the Student Graduate Works at AFIT Scholar. It has been accepted for inclusion in Theses and Dissertations by an authorized administrator of AFIT Scholar. For more information, please contact [richard.mansfield@afit.edu](mailto:richard.mansfield@afit.edu).



POINT SPREAD FUNCTION CHARACTERIZATION  
OF A RADially DISPLACED SCATTERER  
USING CIRCULAR SYNTHETIC APERTURE RADAR

THESIS

Uttam K. Majumder

AFIT/GE/ENG/07-26

DEPARTMENT OF THE AIR FORCE  
AIR UNIVERSITY

**AIR FORCE INSTITUTE OF TECHNOLOGY**

Wright-Patterson Air Force Base, Ohio

APPROVED FOR PUBLIC RELEASE; DISTRIBUTION UNLIMITED

The views expressed in this thesis are those of the author and do not reflect the official policy or position of the United States Air Force, Department of Defense, or the United States Government.

POINT SPREAD FUNCTION CHARACTERIZATION  
OF A RADially DISPLACED SCATTERER  
USING CIRCULAR SYNTHETIC APERTURE RADAR

THESIS

Presented to the Faculty  
Department of Electrical and Computer Engineering  
Graduate School of Engineering and Management  
Air Force Institute of Technology  
Air University  
Air Education and Training Command  
In Partial Fulfillment of the Requirements for the  
Degree of Master of Science

Uttam K. Majumder, B.S.

March 2007

APPROVED FOR PUBLIC RELEASE; DISTRIBUTION UNLIMITED

POINT SPREAD FUNCTION CHARACTERIZATION  
OF A RADially DISPLACED SCATTERER  
USING CIRCULAR SYNTHETIC APERTURE RADAR

Uttam K. Majumder, B.S.

Approved:

/signed/

13 Mar 2007

---

Dr. Michael A. Temple (Chairman)

---

Date

/signed/

13 Mar 2007

---

Capt. Michael A. Saville, Ph.D (Member)

---

Date

/signed/

13 Mar 2007

---

Dr. Michael J. Minardi (Member)

---

Date

*Abstract*

This research effort investigated characterizing the point spread function (PSF) behavior of radially displaced point scatterers using circular synthetic aperture radar (CSAR). For persistent staring radar applications utilizing CSAR for target recognition, it is important to know how a target's PSF behaves as a function of various radar functional parameters and different target positions. Thus far, research has been conducted to understand PSF of a scatterer located at the imaging scene center. An analytic closed-form solution has been derived assuming the scatterer is located at the origin of the CSAR imaging geometry. However, it is difficult to derive an analytic PSF solution for a scatterer that is radially displaced from the imaging scene center. Using the backprojection image formation algorithm, PSF responses are generated at various point target locations. Consistent with previous studies, the three dimensional PSF for a point target located at the image center is cone shaped and serves as the basis for comparing and characterizing the PSFs of radially displaced scatterers. Simulated results show the impulse response of a radially displaced point scatterer is asymmetric and tends to exhibit increased ellipticity as it moves further from the scene center.

## *Acknowledgements*

I am grateful to God for giving me the privilege to complete my Master degree at a world renowned military graduate institution, The Air Force Institute of Technology (AFIT). Throughout three years of part-time study, I encountered a few difficult moments. God helped me to overcome those difficult times by providing encouragement and strength.

I deeply appreciate Dr. Michael J. Minardi and Mr. Edmund G. Zelnio for your graciousness while spending many hours with me on technical discussions. Fellowship with you motivated me to explore the Synthetic Aperture Radar (SAR) research and completion of my Master's thesis. I am very grateful to you for your unconditional support, inspiration and influence on this study.

I am grateful to the AFRL/SNAS Branch Chief Mr. Martin E. Justice for your unwavering support of advanced study. I appreciate Mr. Steven C. Sawtelle of AFRL/SNA for your help. I also appreciate my colleagues and friends for many fruitful discussions on SAR.

I would like to thank the Dayton Area Graduate Studies Institute (DAGSI) for funding a portion of my tuition through a tuition scholarship.

I am thankful to Captain Michael A. Saville to serve as a member of my thesis committee.

I would like to acknowledge my academic and thesis advisor Dr. Michael A. Temple for helping me complete my thesis research. I am very fortunate to have an exceptional advisor like Dr. Temple who provided lots of guidance essential to understanding many concepts I encountered during my study. For all the support Dr. Temple has given me concerning research and publications necessary to succeed in graduate school, I am very grateful.

Uttam K. Majumder

## *Table of Contents*

	Page
Abstract . . . . .	iv
Acknowledgements . . . . .	v
List of Figures . . . . .	viii
List of Tables . . . . .	xi
List of Abbreviations . . . . .	xii
 I. Introduction . . . . .	 1
1.1 Research Problem . . . . .	2
1.2 Research Motivation . . . . .	3
1.3 Thesis Organization . . . . .	4
 II. Background on Synthetic Aperture Radar . . . . .	 5
2.1 Basic Radar Concept . . . . .	5
2.2 SAR Imaging . . . . .	8
2.2.1 Range Imaging . . . . .	10
2.2.2 Cross-range Imaging . . . . .	12
2.3 Stripmap SAR . . . . .	16
2.4 Spotlight SAR . . . . .	17
2.5 Interferometric SAR (IFSAR) . . . . .	17
2.6 Summary . . . . .	20
 III. Circular Synthetic Aperture Radar (CSAR) . . . . .	 21
3.1 CSAR Processing . . . . .	21
3.2 Merits of CSAR Processing . . . . .	22
3.3 CSAR Image Formation Techniques . . . . .	23
3.4 Backprojection Image Formation . . . . .	24
3.5 Summary . . . . .	28
 IV. Data Generation Methodology . . . . .	 29
4.1 Analytic PSF Characteristics . . . . .	29
4.2 Simulated PSF Generation . . . . .	31
4.3 Data Collection Geometry . . . . .	32
4.4 Radar Waveform . . . . .	33
4.5 Summary . . . . .	35



	Page
V. Results and Analysis . . . . .	36
5.1 PSF Characteristics of an Off-center Target . . . . .	36
5.2 PSF Results: Point target at the origin . . . . .	36
5.2.1 2D PSF Responses . . . . .	38
5.2.2 3D Plots of the PSF Responses . . . . .	41
5.3 PSF Results: Radially displaced point target . . . . .	44
5.3.1 2D PSF Responses . . . . .	44
5.3.2 3D plots of the PSF Responses . . . . .	50
5.4 Summary . . . . .	55
VI. Conclusions . . . . .	56
6.1 Research Summary . . . . .	56
6.2 Contribution to SAR research . . . . .	57
6.3 Future Research on Radially Displaced Targets in CSAR . . . . .	57
6.3.1 CSAR response to canonical shapes . . . . .	57
6.3.2 Analytic PSF expression for radially displaced point scatterers . . . . .	58
6.3.3 Detection and ATR algorithms based on PSF response . . . . .	58
Bibliography . . . . .	59

## *List of Figures*

Figure		Page
2.1.	Radar Signal Transmission . . . . .	6
2.2.	2D Radar Data Matrix . . . . .	7
2.3.	Radar Data Cube . . . . .	9
2.4.	Range Doppler Processing . . . . .	9
2.5.	SAR Imaging Geometry and Terminology . . . . .	10
2.6.	SAR Range Imaging . . . . .	10
2.7.	Reconstructed Range Images. . . . .	12
2.8.	Cross-Range Imaging System. . . . .	13
2.9.	Reconstructed Cross-Range Images. . . . .	16
2.10.	Stripmap Data Collection Geometry. . . . .	17
2.11.	Spotlight SAR data collection geometry . . . . .	18
2.12.	IFSAR Data Collection Geometry with Single-pass. . . . .	19
2.13.	IFSAR Data Collection Geometry with two passes. . . . .	19
3.1.	CSAR Processing Geometry . . . . .	22
3.2.	CSAR data in Fourier space . . . . .	23
3.3.	Polar to Rectangular Interpolation . . . . .	24
3.4.	Radon Transform . . . . .	25
3.5.	Backprojection Concept . . . . .	26
3.6.	Backprojection Reconstruction . . . . .	27
4.1.	CSAR Data Collection Geometry. . . . .	32
4.2.	Waveform Representation: Sinc shape. . . . .	33
4.3.	Waveform Representation: Gaussian shape. . . . .	33
4.4.	CSAR image formed using a sinc shaped waveform. . . . .	34
4.5.	CSAR image formed using a gaussian shaped waveform. . . . .	34
5.1.	2D PSF for point scatterer located at the scene center (0,0,0). . . . .	37

Figure		Page
5.2.	2D PSF for the point scatterer located at the scene center (0,0,0). The image plane is 1 meter above the ground plane. . . . .	38
5.3.	2D PSF for the point scatterer located at the scene center (0,0,0). The image plane is 2 meters above the ground plane. . . . .	39
5.4.	2D PSF for the point scatterer located at the scene center (0,0,0). The image plane is 3 meters above the ground plane. . . . .	40
5.5.	$X$ - $Z$ plane cut of the 3D PSF for point scatterer located at the scene center (0,0,0). . . . .	40
5.6.	3D plot of PSF for the point scatterer located at the scene center (0,0,0). The image plane is the ground plane. . . . .	41
5.7.	3D plot of PSF for the point scatterer located at the scene center (0,0,0). The image plane is 1 meter above the ground plane. . .	42
5.8.	3D plot of PSF for the point scatterer located at the scene center (0,0,0). The image plane is 2 meters above the ground plane. .	42
5.9.	3D plot of PSF for the point scatterer located at the scene center (0,0,0). The image plane is 3 meters above the ground plane. .	43
5.10.	Cone shaped 3D PSF for point scatterer located at the scene center (0,0,0). . . . .	43
5.11.	2D PSF for point scatterer displaced 3000 meters along the pos- itive $x$ -axis. The image plane is the ground plane . . . . .	45
5.12.	2D PSF for point scatterer displaced 3000 meters along the pos- itive $x$ -axis. The image plane is 1 meter above the ground plane.	45
5.13.	2D PSF for point scatterer displaced 3000 meters along the pos- itive $x$ -axis. The image plane is 2 meters above the ground plane.	46
5.14.	2D PSF for point scatterer displaced 3000 meters along the pos- itive $x$ -axis. The image plane is 3 meters above the ground plane.	46
5.15.	$X$ - $Z$ plane cut of the 3D PSF for point scatterer displaced 3000 meters along the positive $x$ -axis. . . . .	47
5.16.	2D PSF for point scatterer displaced 5000 meters along the pos- itive $x$ -axis. The image plane is the ground plane. . . . .	48
5.17.	2D PSF for point scatterer displaced 5000 meters along the pos- itive $x$ -axis. The image plane is 1 meter above the ground plane.	48

Figure		Page
5.18.	2D PSF for point scatterer displaced 5000 meters along the positive $x$ -axis. The image plane is 2 meters above the ground plane.	49
5.19.	2D PSF for point scatterer displaced 5000 meters along the positive $x$ -axis. The image plane is 3 meters above the ground plane.	49
5.20.	3D plot of PSF for the point scatterer displaced 3000 meters along the positive $x$ -axis. The image plane is the ground plane.	50
5.21.	3D plot of PSF for the point scatterer displaced 3000 meters along the positive $x$ -axis. The image plane is 1 meter above the ground plane. . . . .	51
5.22.	3D plot of PSF for the point scatterer displaced 3000 meters along the positive $x$ -axis. The image plane is 2 meters above the ground plane. . . . .	51
5.23.	3D plot of PSF for the point scatterer displaced 3000 meters along the positive $x$ -axis. The image plane is 3 meters above the ground plane. . . . .	52
5.24.	3D plot of PSF for the point scatterer displaced 5000 meters along the positive $x$ -axis. The image plane is the ground plane.	53
5.25.	3D plot of PSF for the point scatterer displaced 5000 meters along the positive $x$ -axis. The image plane is 1 meter above the ground plane. . . . .	53
5.26.	3D plot of PSF for the point scatterer displaced 5000 meters along the positive $x$ -axis. The image plane is 2 meters above the ground plane. . . . .	54
5.27.	3D plot of the PSF response for the point scatterer displaced 5000 meters along the positive $x$ -axis. The image plane is 3 meters above the ground plane. . . . .	54

## *List of Tables*

Table		Page
4.1.	Experimental parameters used to characterize PSF of a radially displaced point scatterer . . . . .	29
4.2.	Simulation Parameters for Backprojection Imaging. . . . .	31
5.1.	PSF Characterization. . . . .	37

*List of Abbreviations*

Abbreviation		Page
CSAR	Circular Synthetic Aperture Radar . . . . .	1
ATR	Automatic Target Recognition . . . . .	2
GMTI	Ground Moving Target Indication . . . . .	4
STAP	Space-Time Adaptive Processing . . . . .	8

POINT SPREAD FUNCTION CHARACTERIZATION  
OF A RADially DISPLACED SCATTERER  
USING CIRCULAR SYNTHETIC APERTURE RADAR

## I. Introduction

Synthetic Aperture Radar (SAR) is a revolutionary technology invented by Carl Wiley in 1950. SAR applications benefit both the civilian and military sectors. Examples of SAR applications include environmental monitoring [16], terrain mapping, and surveillance operations. The most important feature of SAR is its capability to form images in day or night under all weather conditions. For staring radar applications, the use of SAR technology is paramount.

Circular Synthetic Aperture Radar (CSAR) is a method for collecting raw SAR data. In CSAR applications, the radar moves in a circular flight path while keeping its mainbeam focused at the center of the ground patch to be imaged. The CSAR process is very similar to inverse SAR (ISAR) where the target rotates and the radar is stationary. Other methods for collecting raw SAR data include stripmap SAR, spotlight SAR and interferometric SAR (IFSAR). In stripmap SAR mode, the radar moves along a straight flight path and illuminates a rectangular strip of the ground during data collection. In spotlight SAR mode, the radar moves along a straight flight path while steering its mainbeam to constantly illuminate a specific ground patch. Lastly, IFSAR mode operates by using data collected from two separate receiver channels that are vertically displaced on the platform. The height differential is then used to map the imaging scene in 3D using interferometry.

Each of the SAR modes described present different operational issues and limitations when forming the desired image. For example, a stripmap image is formed using data collected over limited azimuth look angles. Thus, stripmap images may not be of sufficient quality to permit target identification with a high degree of confidence.

For an automatic target recognition (ATR) system requiring target identification with a higher degree of confidence, CSAR processing represents a viable alternative given it can produce images with resolution less than a wavelength, depending on scatterer persistence throughout the collection interval. Many studies have been conducted that address CSAR image reconstruction [1, 3, 7, 18], with [19] describing the CSAR image reconstruction process in great detail.

### ***1.1 Research Problem***

Wide-angle imaging provides significantly better resolution than other imaging modalities. Higher resolution has proven to provide better target recognition performance for ATR systems. For that reason, CSAR has been used for staring radar applications in which large apertures could be utilized for achieving better cross-range resolution. In previous studies considering wide-angle imaging and point spread functions (PSF), the studies assumed that the target was located at the imaging scene center. Based on this assumption and the assumption that the entire circular path is flown, the behavior of a point target PSF is well understood. Researchers have derived analytic closed-form PSF solutions for a point target located at the center of the imaging geometry [13, 19].

One important issue in CSAR imaging involves understanding target PSF behavior as the target becomes radially displaced from the image scene center. Complete PSF characterization of a specific target (i.e., one comprised of multiple, uniquely located point scattering centers) could lead to enhanced focusing and geolocation of this particular target as it moves through the CSAR imaging geometry.

It is well understood that not all target scattering is point-like and, therefore, additional challenges concerning complex target characteristics (number of dominant scatterers, scattering center location, orientation, etc.) should be investigated; however, these challenges are beyond the scope of this research. Thus, this research focused on characterizing the PSF behavior of a single point scatterer that is first located at the image center and then radially displaced within the scene.



## 1.2 *Research Motivation*

In today's world, the battlefield is becoming more and more complex. This complexity grows as battles move from open field, to forest, to urban areas. Designating targets as belonging to enemy forces is becoming more and more difficult as well, given that military vehicles, civilian vehicles, bicycles, etc., are now commonly used to conduct military operations. Thus, identification of complex targets in complex battle areas is very important and extremely challenging. Persistent staring radar utilizing CSAR represents one promising technology to address the aforementioned issues.

Synthetic Aperture Radar (SAR) is commonly used for imaging and automatic target recognition (ATR) applications. CSAR collections with large apertures (those spanning  $90^\circ$  of azimuth or more) have two properties that potentially make them very useful. First, they can provide resolution in the  $X$ - $Y$  planes that are less than a wavelength and are essentially independent of the bandwidth. Second, the resultant PSFs can provide resolution in three dimensions using a single phase center and a single pass. It is envisioned that a better understanding of PSF characteristics for a radially displaced target could enable an ATR system to fully exploit these two properties.

One significant challenge for CSAR processing is the imaging of large scene sizes. For large scenes, the PSF response can change significantly as the point of interest is radially displaced from scene center. Thus, it is important to understand PSF behavior for all locations in the scene, and in particular, when imaging large scenes.

The fundamental goal of this thesis research is to characterize the PSF response of a radially displaced point target. The research utilized simulation to perform this characterization. The ability to understand PSF behavior for a target located in any position of a large scene is fundamental to understanding the signature of complex targets. This understanding will lead to a better ATR algorithm development for

both target recognition and detection, e.g., ground moving target indication(GMTI) development.

### ***1.3 Thesis Organization***

The rest of this document is divided into five chapters, with each providing specific details on a topic contributing to the research. The topics addressed include: SAR background, CSAR processing, data generation, results and analysis.

Chapter 2 describes SAR image processing concepts to include a definition of range and cross-range resolution. Range and cross-range imaging is outlined. SAR data collection modalities such as stripmap SAR, spotlight SAR, interferometric SAR (IFSAR) have been discussed in great details.

Chapter 3 provides a comprehensive discussion on CSAR processing. Details on an important SAR image formation algorithm, known as convolutional backprojection, are presented in this chapter.

Chapter 4 describes the data generation methodology used to characterize the PSF of radially displaced point scatterers. CSAR data collection geometry is introduced and key CSAR parameters for synthetic data generation are presented, including depression angle, radar center frequency, bandwidth, range from target to the aircraft. Radar waveform selection issues are also discussed.

Chapter 5 provides simulation results and analysis for several scenarios. A baseline PSF response is first considered where the point target is located at the scene center. Both 2D and 3D PSFs are presented for the baseline case. Results for scenarios involving radially displaced point targets are then introduced. Again, both 2D and 3D PSF responses are presented and discussed.

Chapter 6 provides research conclusions and presents recommendations for future research.

## II. Background on Synthetic Aperture Radar

This section describes synthetic aperture radar (SAR) signal and image processing concepts. The SAR signal processing concept is based upon single (e.g. range profile) or multi dimensional radar signal processing. Many books have been written that explain radar signal processing concepts in great details. The radar signal processing concepts presented in this chapter are extracted from books written by Merrill Skolnik [17], Mark Richards [14] and Bassem Mahafza [10]. Several well written SAR monographs have been authored by Mehrdad Soumekh [19], Charles Jakowatz [9] and Walter Carrara [4]. Soumekh [19] provides a very comprehensive signal level understanding of SAR. Hence, the notation, symbols, mathematical equations and pictures used in this section to illustrate SAR signal and image processing concepts follow from Soumekh's book [19]. Since this thesis research focused on CSAR, a limited discussion on basic radar concept has been provided.

### 2.1 Basic Radar Concept

RADAR stands for RAdio Detection And Ranging. A radar system transmits a sequence of pulses which are incident upon targets of interest and reflect back. A receiver records the echoed signal. Time delay between the transmit and receive signal is used to calculate range information. Radar range is calculated using the following equation [10, 14, 17]

$$R = \frac{cT_r}{2}, \quad (2.1)$$

where  $c$  is the speed-of-light and  $T_r$  is round trip travel time of a radar signal.

Figure 2.1 shows the radar signal transmission and reception concept [21]. After signal transmission, the radar system waits for sufficient time to record the echo signal. The waiting period (time) between two consecutive transmitted pulses is called *pulse repetition interval* (PRI). The reciprocal of PRI is called the *pulse repetition*

*frequency* (PRF). Multiple PRIs are necessary to detect two targets unambiguously. The following equation defines maximum unambiguous range [17]

$$R_{un} = \frac{cT_p}{2} = \frac{c}{2f_p}, \quad (2.2)$$

where  $T_p$  is the PRI and  $f_p$  is the PRF.

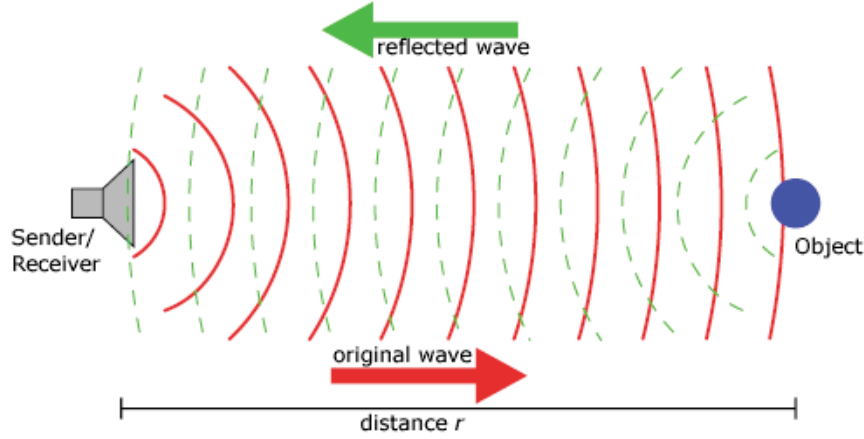


Figure 2.1: Radar signal transmission and reception concept [21].

A series of echoed radar pulses form a coherent processing interval (CPI) or dwell. Each pulse within a CPI is sampled adequately to retrieve meaningful target information. Each sampled point of a pulse is known as range bin, range gate, or resolution cell [14]. Since a radar system samples a pulse as it arrives, range bin is also known as fast time sample and range axis is also known as *fast time* axis. After sampling the first pulse, the next pulse is sampled and the process continues until the last pulse of the CPI is received. Hence, the pulse axis is known as *slow time* axis. In SAR, *slow time* is also known as synthetic aperture axis. Figure 2.2 shows a 2D radar data matrix.

Multiple receive channels provide multiple CPI processing and constitute a data cube. Figure 2.3 shows a 3D radar data cube. The 3D radar data cube concept is illustrated by Mark Richards [14] and provides an easy way of understanding and

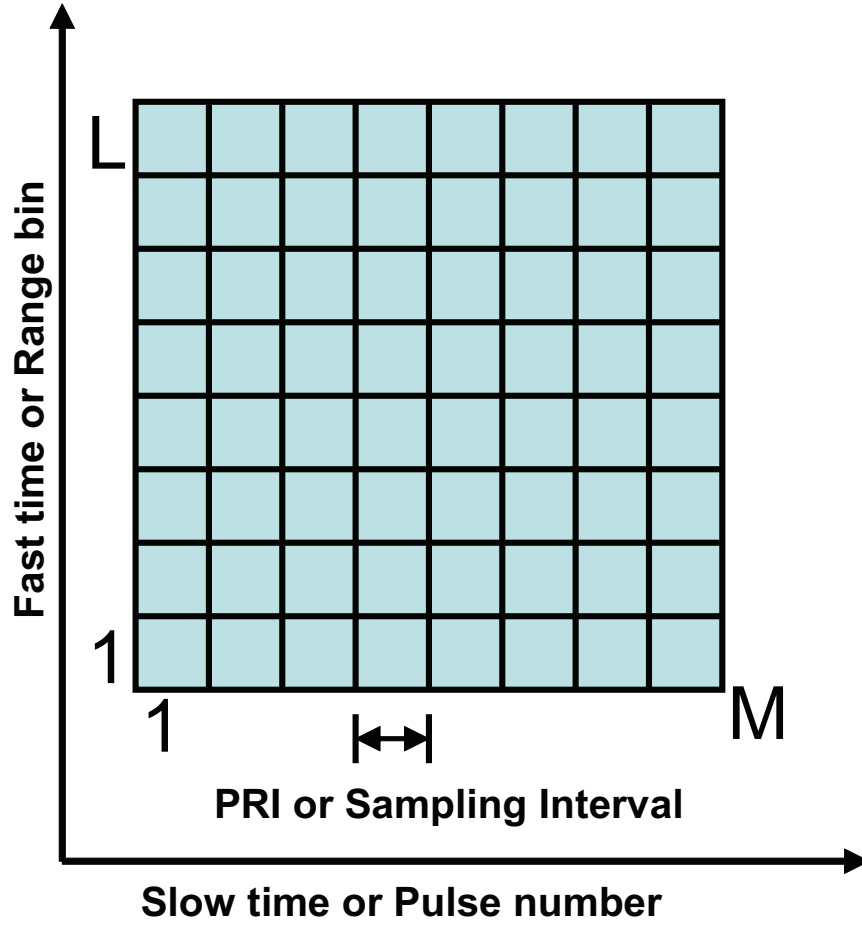


Figure 2.2: 2D Radar Data Matrix. The horizontal axis is the slow time or pulse number axis. It contains  $M$  pulses for a CPI and represents duration of CPI. The vertical axis is the fast time or range axis. It contains  $L$  range bins or fast time samples and represents duration of CPI [14].

remembering several important radar signal processing concepts. For example, 1D filtering or Fourier transform along pulse/slow time axis is called Doppler processing. Doppler processing provides information about moving targets. Figure 2.4 shows Doppler processing concept.

Pulse compression is the 1D convolution along the range axis or fast time axis. To detect targets at a long range, very long pulses are needed. However, a long pulse provides poor range resolution. To mitigate this problem, a frequency or phase modulated signal is transmitted by a radar. This is known as pulse compression process. Pulse compression enables obtaining the high range resolution of a short pulse while using a long pulse.

One dimensional (1D) weighting across antenna receive channels is called beam-forming. Two Dimensional (2D) joint adapting weighting across antenna receive channels and pulse numbers is called space-time adaptive processing (STAP). Finally, 2D matched filtering in slow time and fast time is called synthetic aperture radar (SAR) imaging.

## 2.2 SAR Imaging

The fundamental SAR imaging geometry is shown in Figure 2.5 [15]. In this figure, the aircraft carrying the radar flies a straight flight path with velocity  $v$  at a certain altitude. Slant range is the distance from the radar to the imaging scene center. Azimuth angle  $\phi$  is defined to be the angle around the scene center which encompasses 0 to  $360^\circ$ . Azimuth angle is also known as aspect angle. Elevation angle  $\theta$  is defined to be the angle measured from the ground plane toward the positive  $z$  - axis which encompasses 0 to  $90^\circ$ . The angle between the slant range and the ground plane is a typical measure of the elevation angle. Elevation angle is equivalent to the depression angle. Ground squint angle is the angle between the aircraft's flight path to the projection of the slant range on the ground.

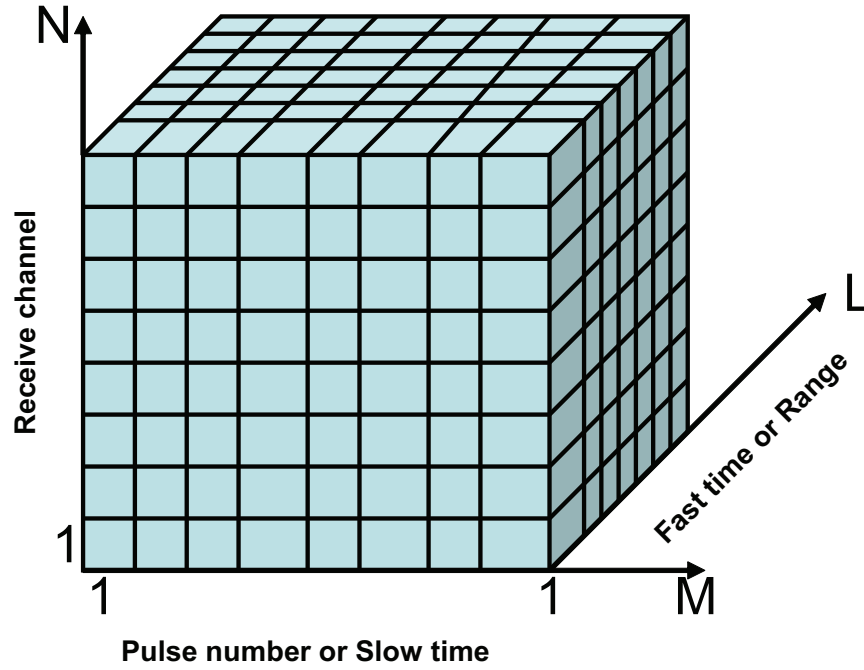


Figure 2.3: Radar Data Cube. The horizontal axis is the pulse number or slow time axis. It contains  $M$  pulses for a CPI. The axis into the page is the fast time or range axis. It contains  $L$  fast time samples. The vertical axis is the number of receive channel. It contains  $N$  receive channels.

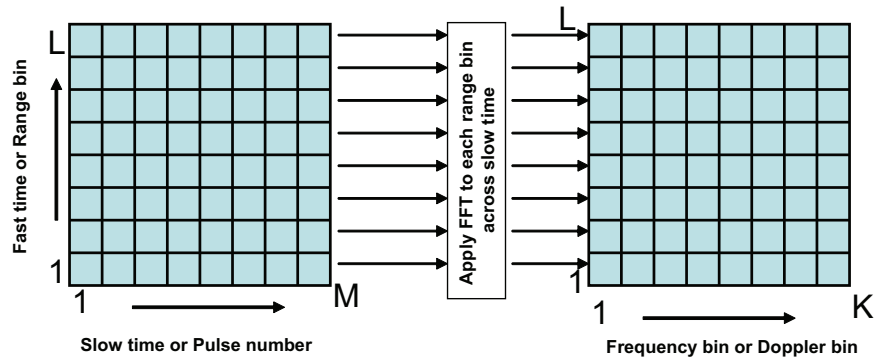


Figure 2.4: Range Doppler Processing concept. By applying Fourier transform along pulse/slow time axis for each range bin, a range Doppler map is created.

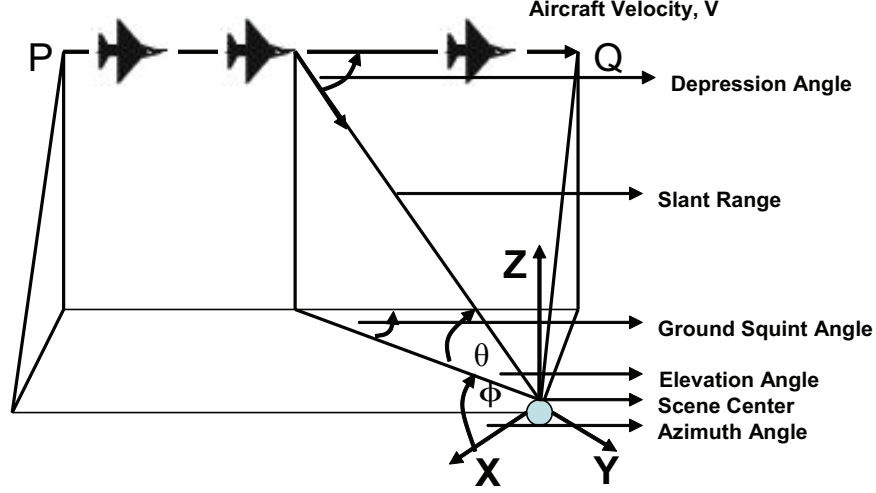


Figure 2.5: SAR imaging geometry and terminology. Azimuth angle  $\phi$  is the angle around the scene center. Elevation angle  $\theta$  is defined to be the angle measured from the ground plane to the  $z$ -axis [15].

*2.2.1 Range Imaging.* System geometry for range imaging is shown in Figure 2.6 [19]. As shown, targets are located at  $X_1$ ,  $X_2$  and  $X_n$ . Each target has a reflectivity of  $\sigma_1$ ,  $\sigma_2$  and  $\sigma_n$ . Total target area coverage is  $2X_0$ . For range imaging, all targets are assumed to be located at the same cross-range location.

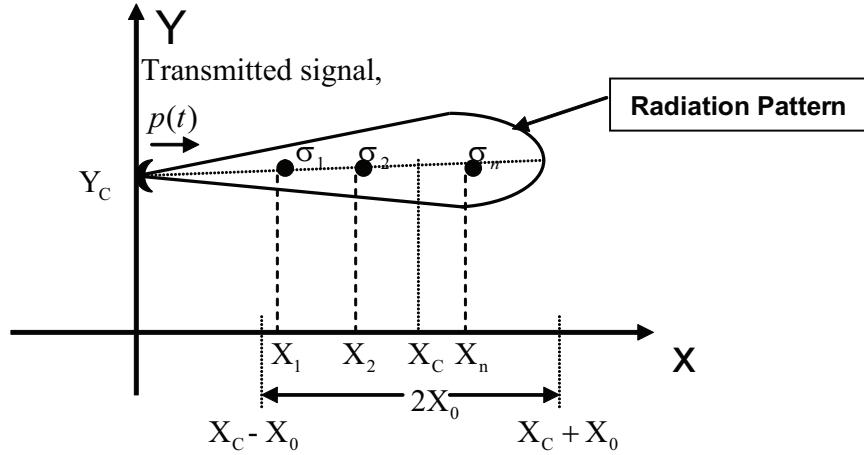


Figure 2.6: SAR range imaging geometry. Targets reside within the finite spatial region  $[X_c - X_0, X_c + X_0]$  or range domain. This is also known as the range swath.  $X_c$  is the scene center. Total target spatial support is  $2X_0$  [19].

Consider  $p(t)$  as the radar transmit signal. Then the received signal  $s(t)$  is characterized by the following equation:



$$s(t) = \sum \sigma_n p\left(t - \frac{2x_n}{c}\right) \quad (2.3)$$

where  $x_n$  and  $\sigma_n$  are the range and reflectivity of the  $n$ th target.

Consider  $S(\omega)$  and  $P(\omega)$  are the Fourier transform of  $s(t)$  and  $p(t)$ , respectively. Therefore, target response function  $f(x)$  can be reconstructed using the following equation:

$$f(x) = F_{(\omega)}^{-1} \left[ \frac{S(\omega)}{P(\omega)} \right] \quad (2.4)$$

where  $F_{(\omega)}^{-1}$  is the inverse Fourier transform operator.

Target reconstruction using (2.4) is known as deconvolution. This method is considered numerically unstable when  $P(\omega)$  is zero. For that reason, matched filtering is used for target reconstruction. Also, matched filtering provides the highest signal to noise ratio (SNR) when the measured signal is corrupted.

Using matched filtering, target response function  $f(x)$  is given by [19]

$$f(x) = \sum_n \sigma_n \text{psf}_n(x - x_n) \quad (2.5)$$

where  $\text{psf}(x)$  is defined by  $F_{(\omega)}^{-1} [|P(\omega)|^2]$ .

*2.2.1.1 Range Resolution.* The SAR range resolution,  $\Delta_x$  is given by following equations:

$$\Delta_x = \frac{c\Delta_t}{2} = \frac{c}{2\omega} \quad (2.6)$$

where  $\Delta_t$  is the sampling interval or PRI and  $\omega$  is the bandwidth in Hertz.

Figure 2.7 illustrates the range image reconstruction via matched filtering. The software used for this simulation is provided by Soumekh [19]. Scene center  $X_c$  is

located at the range 2000 meters. Targets are located at -25, 0, 17.5 and 35 meters from the scene center  $X_c$  (i.e. at the range of 1975, 2000, 2017.5, and 2035 meters). Reflectivity of these targets are 0.8, 1.0, 1.0 and 0.8, respectively. The radar center frequency is 1.0 GHz and the bandwidth is 100 MHz. As shown in Figure 2.7, target responses represent reflectivity used in the simulation.

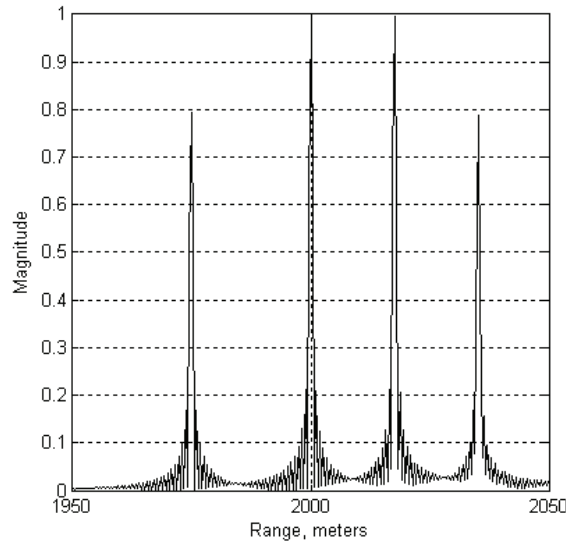


Figure 2.7: Range image reconstruction via matched filtering. Scene center  $X_c$  is located at range 2000 meters. Targets were located at -25, 0, 17.5 and 35 meters from the scene center.

*2.2.2 Cross-range Imaging.* The system geometry for cross-range imaging is shown in Figure 2.8 [19]. In cross-range imaging, the radar stays at a fixed range,  $x$ . The aircraft moves in cross-range axis,  $y$ .

As depicted in Figure 2.8, targets are located at  $Y_1$ ,  $Y_2$  and  $Y_n$ . Each target has a reflectivity of  $\sigma_1$ ,  $\sigma_2$ , and  $\sigma_n$ . Total target area coverage is  $2Y_0$ . Synthetic aperture axis  $u$  extends from  $(-L, L)$ . Consider the case when the radar is located at  $(0, u)$  which is equivalent to  $(x, y)$  in Cartesian coordinate. The radar distance,  $d$  from a target at  $(x, y_n)$  is given by the following equation:

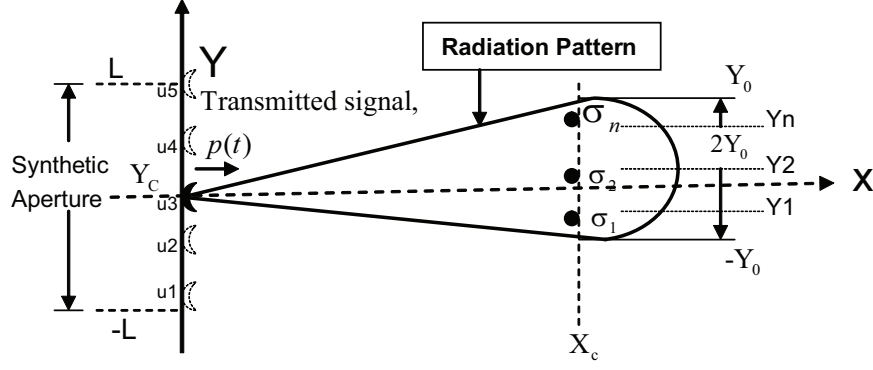


Figure 2.8: Cross-range imaging geometry. Targets reside within the finite target area  $[-Y_0, Y_0]$  in cross-range. Total target cross-range support is  $2Y_0$  [19].

$$d = \sqrt{x^2 + (y_n - u)^2} \quad (2.7)$$

Now assume the radar transmits the following complex signal:

$$p(t) = \exp(j\omega t) \quad (2.8)$$

The measured echo signal from (2.8) is a function of  $u$  which could be expressed by the following equation:

$$s(t, u) = \sum_n \sigma_n p \left[ t - \frac{2\sqrt{x^2 + (y_n - u)^2}}{c} \right] \quad (2.9)$$

For radar frequency  $\omega$ , wave number  $k$  is defined by the following equation:

$$k = \frac{\omega}{c} \quad (2.10)$$

It follows from (2.8) and (2.10) that (2.9) can be rewritten as follows:

$$s(t, u) = \exp(j\omega t) \sum_n \sigma_n \exp \left[ -2j\omega \frac{\sqrt{x^2 + (y_n - u)^2}}{c} \right] \quad (2.11)$$

$$s(t, u) = \exp(j\omega t) \sum_n \sigma_n \exp \left[ -j2k \sqrt{x^2 + (y_n - u)^2} \right] \quad (2.12)$$

After baseband conversion using:

$$s(\omega, u) = s(t, u) \exp(-j\omega t) \quad (2.13)$$

The signal in (2.12) can be rewritten as:

$$s(\omega, u) = \sum_n \sigma_n \exp[-j2k \sqrt{x^2 + (y_n - u)^2}] \quad (2.14)$$

Now, let  $s_n(\omega, u) = \exp[-j2k \sqrt{x^2 + (y_n - u)^2}]$ . Then the baseband signal in (2.14) is represented by:

$$s(\omega, u) = \sum_n \sigma_n s_n(\omega, u) \quad (2.15)$$

The Fourier transform of the phase-modulated baseband signal in (2.14) is given by the following equation [19].

$$s_n(\omega, k_u) = \sigma_n \exp(-j\sqrt{4k^2 - k_u^2} x_n - jk_u y_n) \quad (2.16)$$

where  $k_u$  is the spatial frequency of  $u$  and  $k_u \in [-2k, 2k]$ .  $k_u$  is also known as the slow-time or Doppler domain [19].

Let  $s(\omega, k_u)$  be the sum of the spatial Fourier transform of the individual signals  $s_n(\omega, k_u)$ . In cross-range imaging, all the targets are located at same range value. Therefore,  $x_n = X_c$ . Hence (2.16) can be rewritten as follows:

$$s(\omega, k_u) = \sigma_n \exp(-j\sqrt{4k^2 - k_u^2}X_c - jk_u y_n) \quad (2.17)$$

It can be shown that the spatial Fourier transform of the reference signal with respect to the synthetic aperture  $u$  is the following [19]:

$$s_0(\omega, k_u) = \exp(-j\sqrt{4k^2 - k_u^2}X_c) \quad (2.18)$$

where  $k_u \in [-2k, 2k]$  and zero otherwise.

Using matched filtering, the target function  $f(y)$  in cross-range can be constructed per the followings:

$$F(k_y) = s(\omega, k_u)s_0^*(\omega, k_u) \quad (2.19)$$

$$F(k_y) = \sum_n \sigma_n \exp(-jk_u y_n) \quad (2.20)$$

$$f(y) = F_{(k_y)}^{-1}[F(k_y)] \quad (2.21)$$

where  $F_{(k_y)}^{-1}$  is the inverse Fourier transform operator and  $s_0^*$  is the complex conjugate of  $s_0$ .

$$f(y) = \sum_n \sigma_n p s f_n(y - y_n) \quad (2.22)$$

Figure 2.9 shows cross-range image reconstruction via matched filtering. Again, software used for this simulation is provided by Soumekh [19]. Scene center  $Y_c$  is located at  $y = 0$  meters. Targets are located at -50, -25, 25 and 25 meters from the scene center. Reflectivity of these targets are 0.8, 1.0, 1.0 and 0.8, respectively. The radar center frequency is 1.0 GHz and the bandwidth is 200 MHz. As shown in Figure 2.9, target responses represent reflectivity used in the simulation.

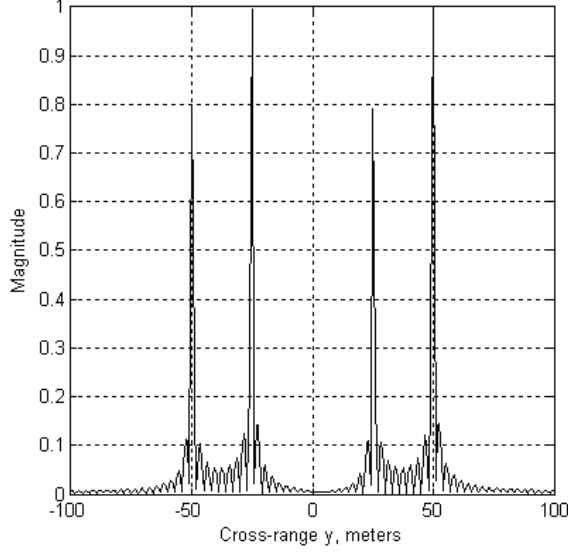


Figure 2.9: Cross-range image reconstruction via matched filtering. Scene center  $Y_c$  is located at  $y = 0$  meters. Targets are located at -50, -25, 25 and 25 meters from the scene center.

*2.2.2.1 Cross-range Resolution.* The SAR cross-range resolution  $\Delta_y$  is given by following equation [19]:

$$\Delta_y = \frac{\lambda}{4} \quad (2.23)$$

where  $\lambda = \frac{2\pi}{k}$  is the wavelength of radar center frequency.

### 2.3 Stripmap SAR

Stripmap SAR was the first SAR imaging method invented in 1950s and is also known as side-looking SAR. In stripmap SAR mode, the radar moves along a straight flight path and illuminates a strip of the ground during data collection.

Fundamental Stripmap imaging geometry is shown in Figure 2.10 [19]. Radar carrying the aircraft flies along the cross-range maintaining a fixed range. Data is collected and image is formed. Some image formation algorithms (e.g. Fresnel approximation) are not suitable for stripmap SAR processing [19].

For some applications it is important to scan some areas of interest quickly to detect target presence. Based on the finding a target is present, the radar operator may employ a high resolution SAR (e.g. Spotlight Mode SAR) system for obtaining more detailed target information. Stripmap SAR is used for these kind of applications.

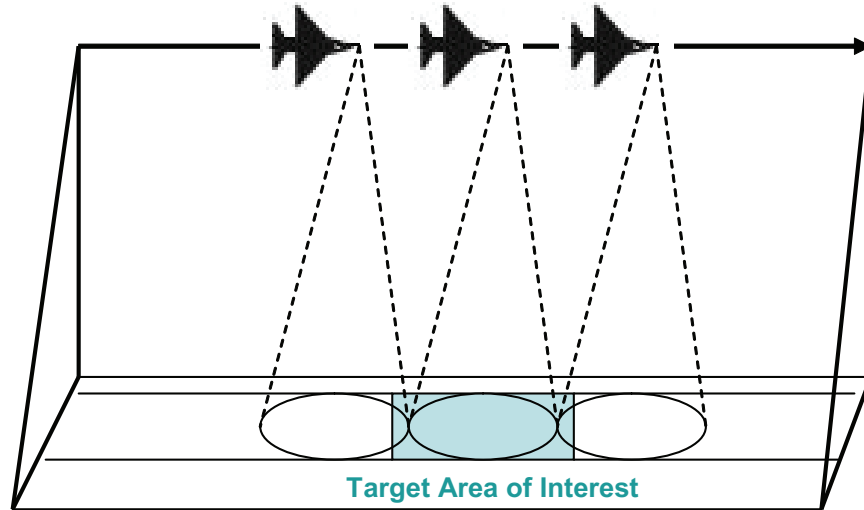


Figure 2.10: Stripmap data collection geometry. Radar carrying the aircraft flies along the cross-range maintaining a fixed range. Data is collected and image is formed [19].

## 2.4 *Spotlight SAR*

In spotlight SAR mode, the radar moves along a straight flight path while steering its mainbeam to constantly illuminate a specific ground patch. SAR spotlight mode imaging geometry is shown in Figure 2.11 [19].

The radar carrying aircraft flies in the cross-range direction ( $y$ -axis) while maintains the fixed range( $x$ -axis). Mechanical or electronic beam steering is used to focus radiation pattern on the same target area [19]. Spotlight SAR data collection enables high resolution imaging capabilities.

## 2.5 *Interferometric SAR (IFSAR)*

Interferometric SAR (IFSAR) mode operates by using data collected from two separate receiver channels that are vertically displaced. The height differential is then

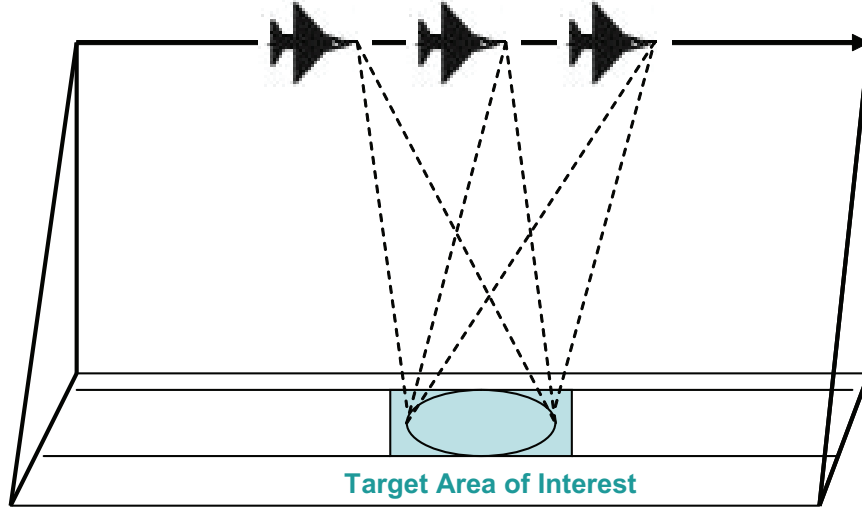


Figure 2.11: Spotlight SAR data collection geometry. The radar carrying aircraft moves along a straight flight path while steering its mainbeam to constantly illuminate a specific ground patch [19].

used to map the imaging scene in 3D using interferometry. Two different methods of IFSAR data collection are found in literature. Jakowatz [9] describes these two methods as single-pass and two-pass interferometry.

Single-pass IFSAR data collection geometry is shown in Figure 2.12. In this method, two receivers reside on the same aircraft with a small vertical separation. Two images can be formed at the same time and a 3D terrain map can be generated. Single-pass IFSAR provides better registration accuracy for interferometric processing and is considered to be very useful for moving target indication (MTI) applications [9].

Two-pass IFSAR data collection geometry is shown in Figure 2.13. In this case, the radar first collect data at an altitude,  $A_1$ . Then collect data at a lower altitude,  $A_2$ . Though the aircraft flies at different altitudes, it tries to maintain the same orbit. This helps image registration accuracy. In general, two-pass IFSAR collection and processing is not as easy as single-pass IFSAR collection and processing. Two-pass IFSAR collection is considered to be useful for change detection (CD) application and measuring terrain motion [9].



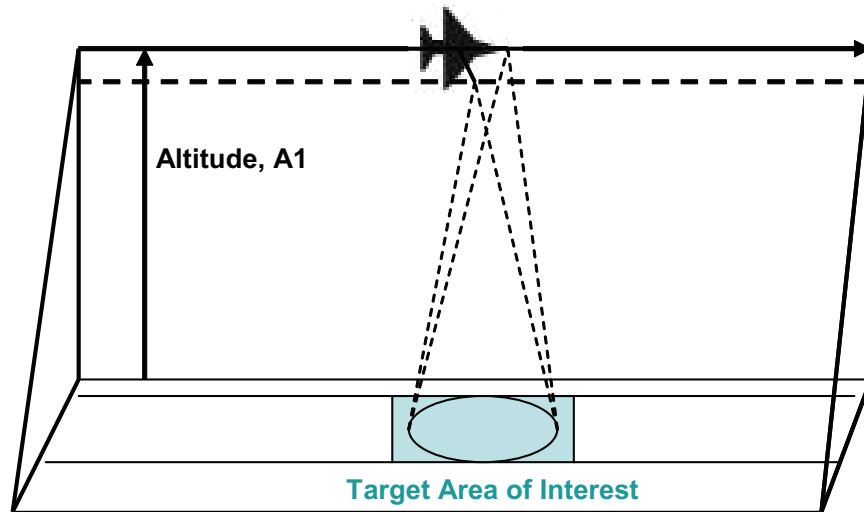


Figure 2.12: IFSAR data collection geometry with single-pass. In this collection, two receivers are separated vertically on the same platform [9].

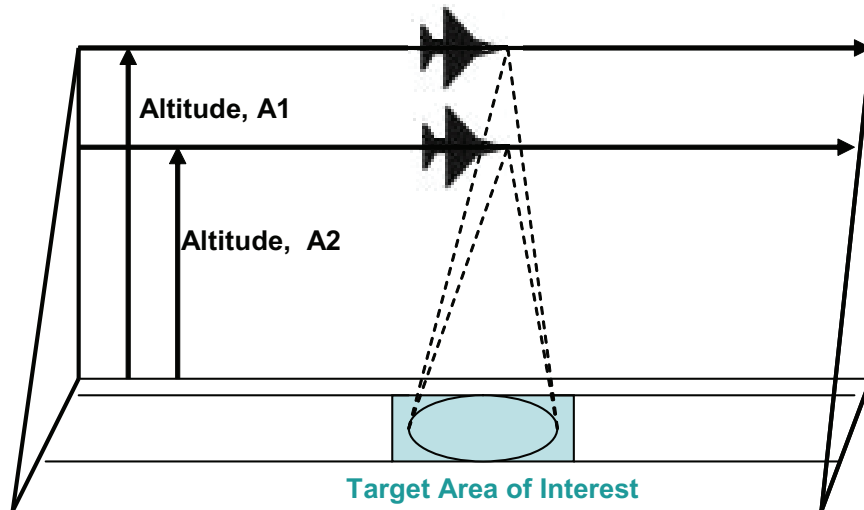


Figure 2.13: IFSAR data collection geometry with two-pass interferometry. In this case, the radar first collects data at an altitude  $A1$ . Then data is collected at a lower altitude  $A2$ . In both altitudes, the platform maintains the same orbit [9].

## ***2.6 Summary***

This section surveys SAR signal and image processing concepts. The basic radar operating concept was presented. Radar signal processing using a radar data cube has been illustrated. SAR terminology and data collection geometry have been discussed. SAR range and cross-range imaging have been developed. Finally, a pictorial description of SAR data collection modalities such as stripmap SAR, spotlight SAR and interferometric SAR (IFSAR) is illustrated.

### III. Circular Synthetic Aperture Radar (CSAR)

This chapter describes circular synthetic aperture radar (CSAR) data collection and processing concepts. Benefits of CSAR data collection have been discussed. A very important CSAR image formation algorithm is the backprojection algorithm. Principally, two different backprojection algorithms can be found in the literature; one is called convolution backprojection (CBP) [2, 5, 6, 20] and the other is called the backprojection filtering (BpjF) [22]. In this chapter, the CBP algorithm will be presented.

#### 3.1 CSAR Processing

SAR data collection modalities such as stripmap SAR, spotlight SAR and interferometric SAR (IFSAR) were described in the previous chapter and use a radar trajectory that is a straight flight path. These data collection modalities are known as *linear* SAR [19]. SAR data collection using a circular flight path is known as circular SAR (CSAR).

In CSAR, the radar moves around a circular flight path while steering its main-beam to constantly illuminate a specific ground patch. Antenna steering is accomplished either mechanically or electronically. CSAR data collection can be viewed as spotlight SAR data collection. However, the difference is that in CSAR the data is collected using a circular path while in spotlight SAR data is collected using a straight flight path.

CSAR data collection geometry is presented in Figure 3.1. This circular path span is from 0 to 360° which is known as azimuth coverage or aspect angle,  $\phi$ . The line of sight (LOS) distance from the radar to the imaging scene center is the *slant range*. The angle between the slant range to the ground plane is called the elevation or depression angle,  $\theta$ .

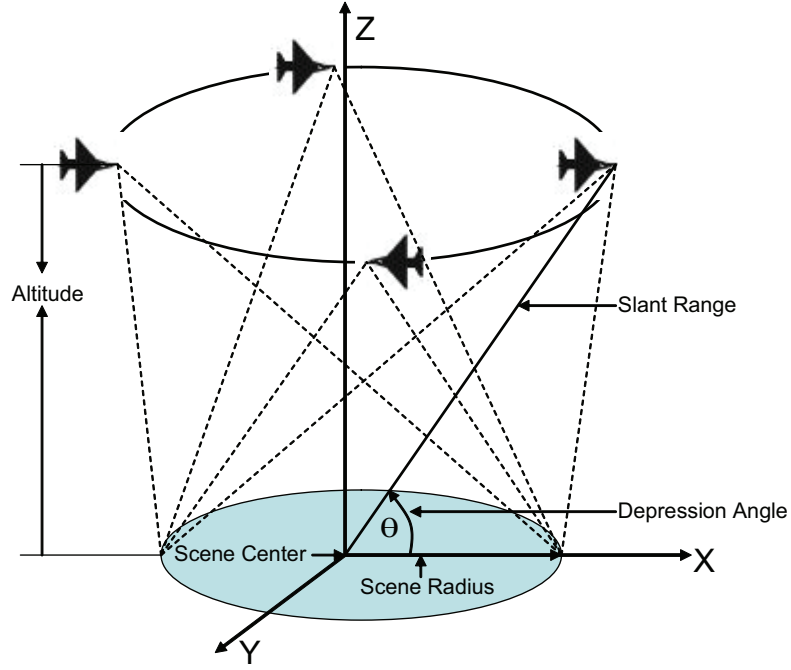


Figure 3.1: Circular SAR (CSAR) data collection geometry. The aircraft carrying the radar flies around a scene of interest. The radar radiation pattern remains constant on the scene.

### 3.2 Merits of CSAR Processing

In linear SAR, an image is formed using data collected over limited azimuth look angles. This imposes two problems for ATR algorithm development. First, images may not be of sufficient quality to permit target identification with a high degree of confidence (e.g. identification of a school bus vs. military vehicle). Second, depending on the angular orientation of the target in the scene, it will be difficult to determine the target type (e.g. identification of various military vehicle of similar types) [19].

CSAR processing provides one solution to the aforementioned problems. First, it is well understood that SAR azimuth resolution (cross-range resolution) is dependent on the length of synthetic aperture [19]. Larger apertures improve cross-range resolution. CSAR enables large aperture sizes by steering the antenna for a long period and therefore provides finer azimuth resolution than *linear* SAR [4].

CSAR has the advantage of imaging the scene from multiple viewing angles. This flexibility is very powerful because many target scattering responses depend on

the observation angle. Hence, CSAR imaging from multiple viewing angles could provide target detection and identification capability with high degree of confidence.

### 3.3 CSAR Image Formation Techniques

The two most common algorithms for CSAR image processing are the polar format algorithm (PFA) and backprojection. Data collected by CSAR systems is called Fourier space or K-space data and resides on an annular grid as shown in Figure 3.2 [5].

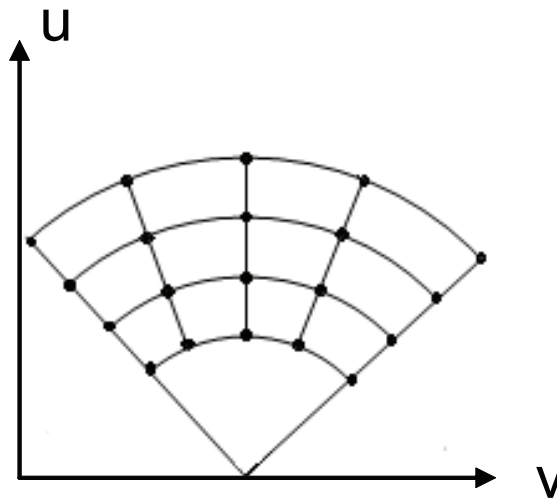


Figure 3.2: CSAR data representation in Fourier domain or K-space [5].

K-space data is related to image data through the Fourier transform. Therefore, to form an image, 2D FFT is applied to the K-space data. However, before applying the 2D FFT, an FFT based imaging method (such as PFA) needs to inscribe a rectangular grid within the annular region as shown in Figure 3.3. This is called polar-to-rectangular (Cartesian) coordinate conversion of K-space data and is accomplished by applying a 2D interpolation on the K-space data. Two major drawbacks of the PFA includes: (1) all radar data must be available from the sensed scene to apply polar to rectangular conversion, and (2) interpolation inaccuracy leads to degraded image quality.

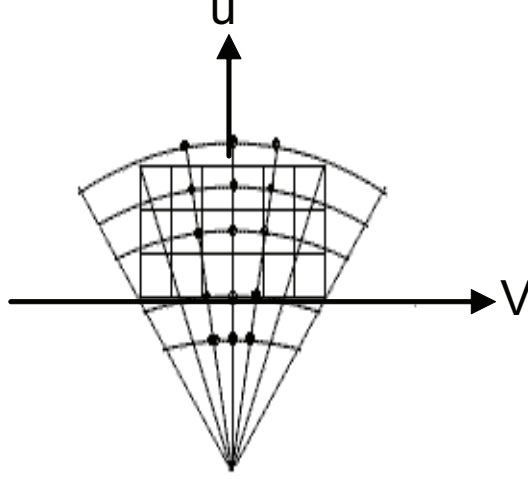


Figure 3.3: Polar to rectangular coordinate interpolation [5].

Backprojection image formation uses K-space data directly and does not require polar to rectangular conversion. Also, all radar data need not be available from the sensed scene to start the image formation process. Further, the quality of images formed by backprojection is superior to that of the PFA. Hence, images formed using backprojection are considered the *Gold Standard* for CSAR processing.

### 3.4 Backprojection Image Formation

The backprojection algorithm was conceived in the field of computer-aided tomography (CAT). Later, it was found that SAR image reconstruction is mathematically similar to CAT and the researchers developed backprojection for SAR [5]. Two variations of backprojection are found in literature: convolution backprojection (CBP) and backprojection filtering (BpjF) [22]. Some papers refer CBP as filtered backprojection (FBP) or factored backprojection (FBP) [20].

In CBP, convolution with a kernel function is accomplished on each projection. The result is then backprojected to a grid. In the BpjF method, first backproject the projections on a image grid. Then the backprojected image is filtered. This filtering

process in BpjF introduces image reconstruction inaccuracy [22]. Hence CBP is the preferred method for backprojection.

The Radon transform is fundamental to backprojection. The Radon transform is described here as excerpted from the book by Jain [8]. Figure 3.4 illustrates the Radon transform concept. The Radon transform maps spatial domain  $(x, y)$  to the  $(s, \theta)$  domain [8]. Each point in the  $(s, \theta)$  space is a line in the spatial domain  $(x, y)$ . The relationships between Cartesian  $(x, y)$ , Polar  $(r, \phi)$  and Radon  $(s, \theta)$  coordinates are given by the following equations:

$$x = r \cos \phi \quad (3.1)$$

$$y = r \sin \phi \quad (3.2)$$

$$s = r \cos(\theta - \phi) \quad (3.3)$$

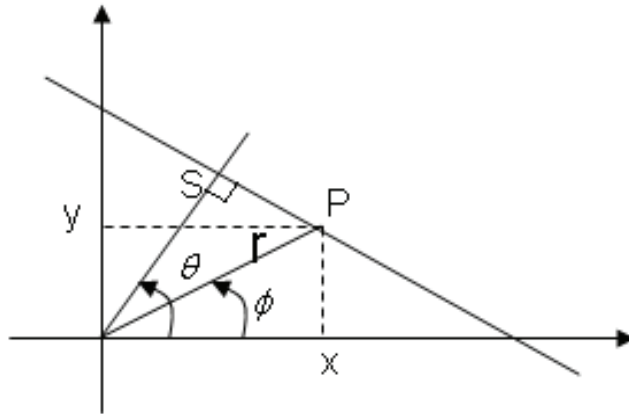


Figure 3.4: Radon transform concept. Radon transform maps spatial domain  $(x, y)$  or polar coordinate  $(r, \phi)$  into the  $(s, \theta)$  space [8].

From the Radon transform, backprojection is defined by the following equations in spatial domain and polar coordinate respectively:

$$f(x, y) = \int_0^\pi g(x \cos \theta + y \sin \theta, \theta) d\theta \quad (3.4)$$

$$f(r, \phi) = \int_0^\pi g(r \cos(\theta - \phi), \theta) d\theta \quad (3.5)$$

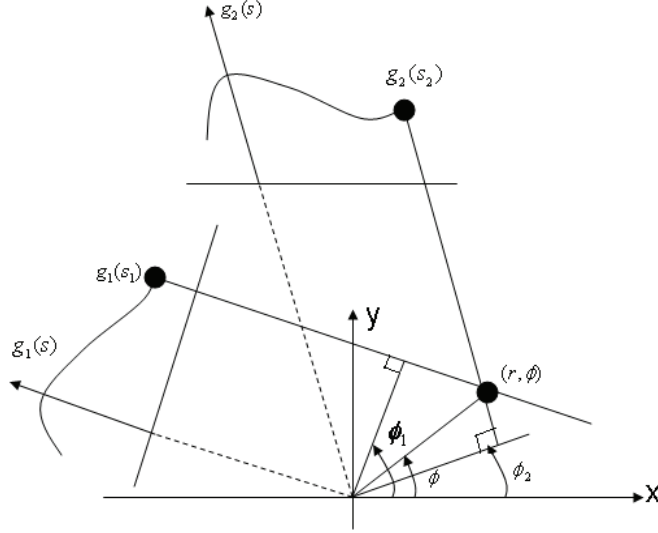


Figure 3.5: Backprojection at pixel location  $(x, y)$  or  $(r, \phi)$  from two projections  $g_1$  and  $g_2$  [8].

The analytic expressions above indicate that backprojection is the summation or integration of rays that pass through a point  $(x, y)$  or  $(r, \phi)$ . In SAR, each ray represents a range profile generated from a radar received signal or pulse. Figure 3.5 shows the backprojection concept using two projections  $g_1$  and  $g_2$ .

Consider,  $g(s, \theta) = g_1(s) + g_2(s)$ . Then the backprojection at  $(r, \phi)$  is given by:

$$f(r, \phi) = g_1(s_1) + g_2(s_2) \quad (3.6)$$

where  $s_1 = r \cos(\theta_1 - \phi)$  and  $s_2 = r \cos(\theta_2 - \phi)$

Figure 3.6 is a visual depiction of the backprojection image formation process. As discussed earlier, rays or pulses from all different directions are backprojected



onto a rectangular grid. Summation of the intensity on each grid is the resulting pixel value.

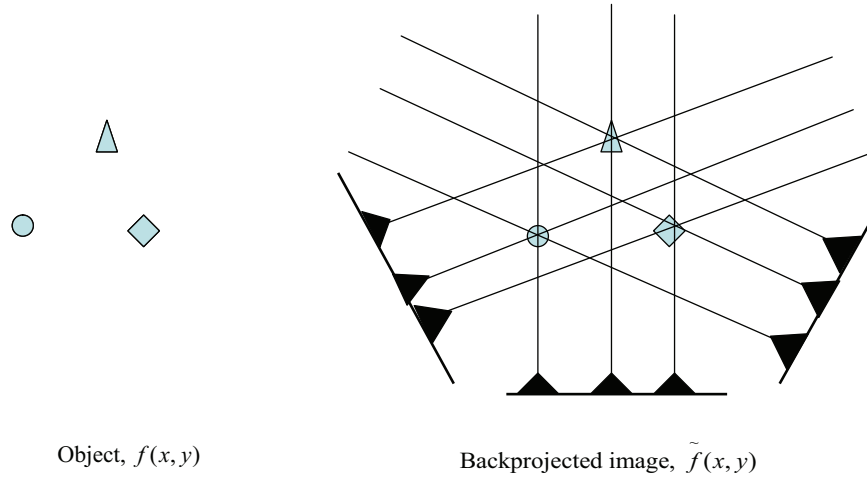


Figure 3.6: Backprojection image reconstruction. Projections from all directions are accumulated to form an image of the objects [8].

Having presented the backprojection concept from the view of a Radon transform, the following is an analytic description of synthetic aperture radar (SAR) convolution backprojection (CBP). CBP can be derived from the 2D Fourier transform. For a scene with ground reflectivity of  $g(x,y)$ , the 2D Fourier transform is defined by the following equations [5]:

$$G(u, v) = \iint_S g(x, y) e^{-j(ux + vy)} dx dy \quad (3.7)$$

$$g(x, y) = \frac{1}{(2\pi)^2} \iint_T G(u, v) e^{j(ux + vy)} du dv \quad (3.8)$$

where  $S$  is the support region of the function  $G(u, v)$  and  $T$  is the support region of the function  $g(x, y)$ . Consider  $(\omega, \theta)$  is the representation of polar coordinates on the  $(u, v)$  grid shown in Figure 3.3. Then  $G(\omega, \theta)$  represents the value of  $G(u, v)$  along a line with an angle  $\theta$  along the  $u$ -axis.

Hence, reconstructed image  $g_{bp}$  on the polar coordinate is given by the following equation [5]:

$$g_{bp}(x, y) = \int_{-\theta/2}^{\theta/2} \int_{\omega_1}^{\omega_2} G(\omega, \theta) e^{-jw(x \cos \theta + y \sin \theta)} |\omega| d\omega d\theta \quad (3.9)$$

where  $\omega$  is the radar frequency and  $\theta$  is the projection angle.

From the above equation, SAR image reconstruction using CBP can be viewed as two steps process. First, each radial line at an angle  $\theta$  is multiplied by the Jacobian,  $|\omega|$ . This is the convolution step since multiplication in Fourier space is equivalent to convolution in time domain. This result is then backprojected onto an image grid.

### 3.5 Summary

In this chapter the circular synthetic aperture radar (CSAR) data collection concept has been presented. Benefits of CSAR processing have been discussed. Finally, an important CSAR image formation technique, the backprojection algorithm concept, has been illustrated.

## IV. Data Generation Methodology

This chapter describes the data generation methodology used to characterize PSF responses of radially displaced scatterers. The SAR data collection scenario simulated for this research is the CSAR collection method. Data is collected for full azimuth coverage of 0 to  $360^\circ$  by placing a point target at the imaging scene center (0,0,0). Similarly, data is collected by placing a point target at a radially displaced location from the imaging scene center. In the synthetic data generation process, motion compensation which is a phase correction/adjustment of collected data was unnecessary. However, motion compensation is essential for airborne SAR data collection systems given that aircraft motion distorts signal phase. Details of PSF characteristics, simulated PSF generation, CSAR data collection and geometry, and radar waveform selection are addressed in the following sections.

### 4.1 Analytic PSF Characteristics

Soumekh [19] provides an analytic expression for the 2D PSF of a point target located at the origin, i.e.  $(x_n, y_n) = (0, 0)$ . The 2D PSF is given by:

Table 4.1: Experimental parameters used to characterize PSF of a radially displaced point scatterer. In this table,  $d_r$  represents the radial displacements of the point target along the positive  $x$ -axis in the scene,  $h$  represents location of the image plane above the ground plane where  $h = 0$  is the ground plane and  $\theta_z$  is the depression angle.

Parameters	Experimental Range
$d_r$ (radial displacement)	0, 3000, 5000 m
$h$ (image plane height)	0, 1, 2, 3 m
$\theta_z$ (depression angle)	$15^\circ$ , $30^\circ$ , $45^\circ$

$$f_n(x, y) = \rho_{max} \frac{J_1(r \cdot \rho_{max})}{r} - \rho_{min} \frac{J_1(r \cdot \rho_{min})}{r} , \quad (4.1)$$

$$r = \sqrt{x^2 + y^2} , \quad (4.2)$$

$$\rho_{max} = 2k_{max} \cos(\theta_z) , \quad (4.3)$$

$$\rho_{min} = 2k_{min} \cos(\theta_z) , \quad (4.4)$$

where  $J_1$  is a first-order Bessel function of the first kind,  $r$  is the scene radius,  $k_{max}$  is maximum wave number of radar signal,  $k_{min}$  is minimum wave number of radar signal, and  $\theta_z$  is average depression angle of the target area.

The 3D PSF of a target located at the scene center (0,0,0) is given by the following equation [13]:

$$f(x, y, z) = \frac{2\pi \sin(\theta_z)}{3} (k_2^3 - k_1^3) \quad (4.5)$$

where  $k_1$  and  $k_2$  are defined by  $\frac{2\pi f_1}{c}$ ,  $\frac{2\pi f_2}{c}$  respectively and  $f_1$ ,  $f_2$  denote minimum and maximum radar operating frequencies.

The analytic expressions in (4.1) and (4.5) show that point target PSF behavior is a function of radar frequency and depression angle. Since analytic PSF expressions for radially displaced point targets are difficult to obtain [19], this study focuses on PSF characterization via computer simulation.

The PSF of a radially displaced point scatterer can be characterized as

$$\text{psf} = f(d_r, h, \theta_z) \quad (4.6)$$

where  $d_r$  is the radial displacement of the point target,  $h$  is the image plane height above the ground and  $\theta_z$  is the depression angle.

Characterization is an observation of changes in the PSF for values according to the Table 4.1 parameters. For the on-center target ( $d_r = 0$  m), the observation

Table 4.2: Simulated parameters used in backprojection imaging. A bandwidth  $\Delta\omega$  of 0.5 GHz provides a range resolution  $\Delta_r$  of 0.3 m, a center frequency of  $f_0$  2.5 GHz provides a wavelength  $\lambda$  of 0.12 m.

Parameters	Value
$\Delta\omega$ (bandwidth)	0.5 GHz
$f_0$ (center frequency)	2.5 GHz
$\lambda$ (wavelength)	0.12 m
$r$ (scene radius)	7000 m
$A$ (sensor altitude)	7000 m
$\theta_z$ (depression angle)	45°
$\Delta_r$ (range resolution)	0.3 m

includes the PSF response is circular and symmetric about the  $z$ -axis or image plane height  $h$ . For the radially displaced target ( $d_r = 3000$  m and 5000 m), the observation includes the PSF response is elliptic and asymmetric about the  $z$ -axis or image plane height  $h$ .

## 4.2 Simulated PSF Generation

Table 4.2 provides the simulation parameters. Parameters are chosen for convenience. However, other parameters can be chosen as well. Simulations were conducted by placing a point scatterer at the imaging scene center and forming an image (PSF) of the scatterer using a backprojection imaging algorithm. The simulations were then run using a radially displaced point scatterer, i.e., a point scatterer displaced from the imaging center along the positive  $x$ -axis by a predetermined distance. Simulations were run for these two cases using a depression angle of  $\theta_z = 45^\circ$ , bandwidth of  $\Delta\omega = 0.5$  GHz and azimuth coverage of 0 to 360°. A bandwidth of  $\Delta\omega = 0.5$  GHz provides a range resolution of  $\Delta_r \approx 0.3$  meters. A center frequency of  $f_0 = 2.5$  GHz was used and corresponds to a wavelength of  $\lambda = 0.12$  m.

Backprojection image formation was accomplished by coherently summing all collected returns for a given depression angle using a full azimuth span. Images

formed using the full  $360^\circ$  azimuth span provide the greatest amount of target information/image detail because the target has been observed from all aspect angles.

### 4.3 Data Collection Geometry

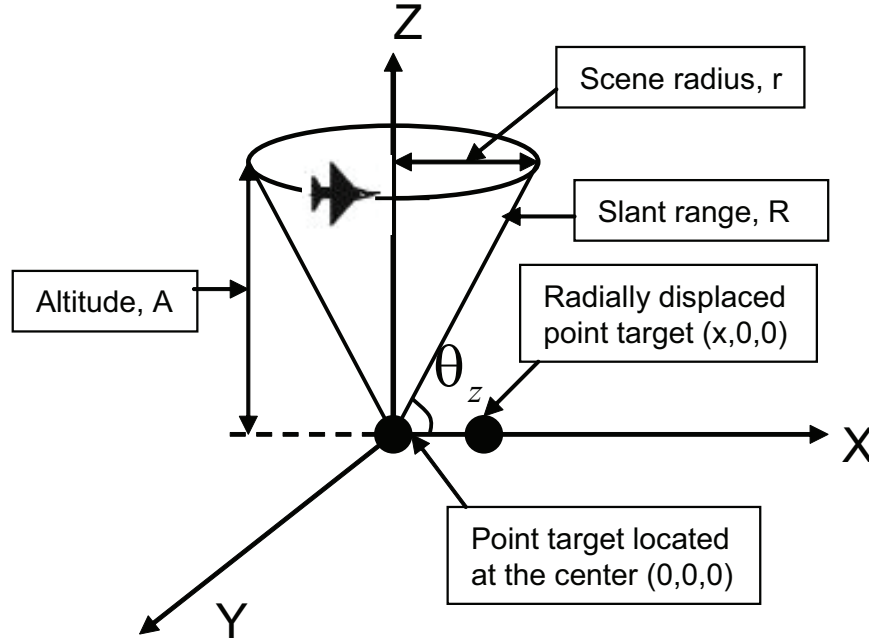


Figure 4.1: CSAR collection and imaging geometry. CSAR equipped aircraft flies in a circular path of radius 7000 m at an altitude of 7000 m from the ground plane.

The simulated CSAR imaging geometry is shown in Fig. 4.1. As indicated, the CSAR equipped aircraft flies a circular path around the  $z$ -axis at a depression angle  $\theta_z$  measured from the  $X$ - $Y$  plane. For this data collection, depression angle  $\theta_z$  is set to  $45^\circ$ . The aircraft flies in a circular path of radius  $r = 7000$  m at an altitude  $A = 7000$  m from the ground plane. Slant range  $R$  from the image scene center  $(0,0,0)$  to the aircraft is approximately 9900 m.

Data was collected over an azimuth span of 0 to  $360^\circ$  under two conditions, including: (1) a point target at the origin  $(0,0,0)$  and (2) a radially displaced point target located at 3000 m and 5000 m along the positive  $x$ -axis.

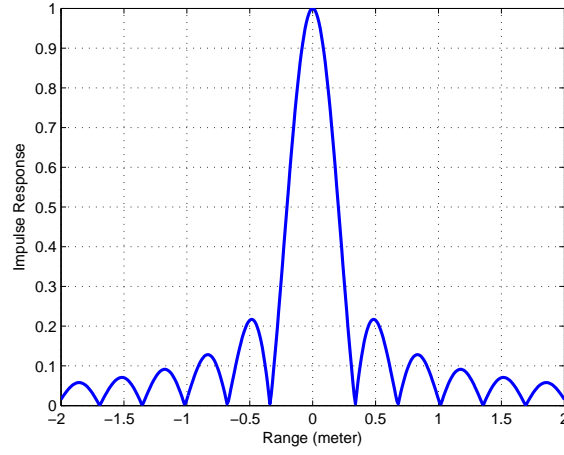


Figure 4.2: Sinc shaped compressed radar waveform.

#### 4.4 Radar Waveform

Time domain signal processing was used for all data generated in support of this study. In other words, frequency domain signal representation and comprehensive waveform design, analysis, and pulse compression methods are not employed. The radar antenna parameters, beamwidth and polarization, have not been considered for the simulation.

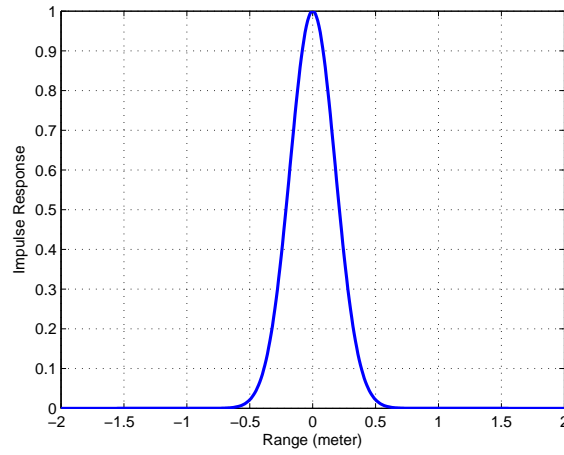


Figure 4.3: Gaussian shaped compressed radar waveform.

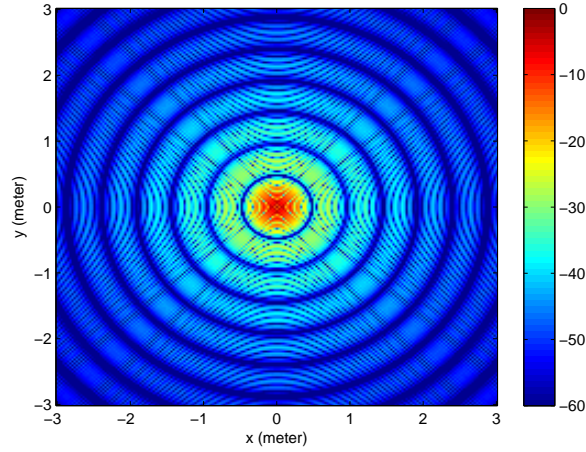


Figure 4.4: CSAR image formed using a sinc shaped compressed radar waveform.

For an azimuth span of 0 to  $360^\circ$ , one radar pulse was transmitted every  $0.5^\circ$ . Thus 720 pulses were transmitted and received by the radar. Two different compressed waveforms have been used to study radar waveform impact on target signature: one is a sinc shaped waveform and the other is the Gaussian shaped waveform. Figure 4.2 and Fig. 4.3 show sinc and Gaussian shaped waveforms, respectively. Figure 4.4 and Fig. 4.5 show two CSAR images formed using each of the aforementioned waveforms.

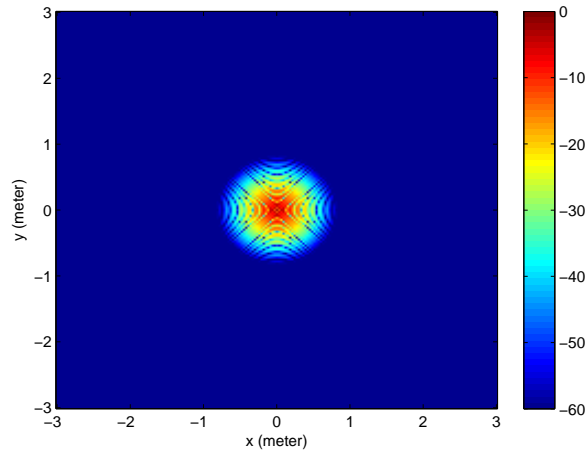


Figure 4.5: CSAR image formed using a gaussian shaped compressed radar waveform.



Since a sinc shaped waveform represents a more realistic radar waveform model for a practical radar system, the Gaussian shaped waveform is not used for data generation.

#### **4.5 Summary**

This chapter outlines the data generation method for PSF characterization. Data is collected over an azimuth span of 0 to 360° by placing a point scatterer at the imaging scene center (0,0,0) as well as, by placing the point scatterer in a radially displaced along the positive  $x$ -axis. Key CSAR parameters for this simulation include a bandwidth of  $\Delta\omega = 0.5$  GHz, center radar frequency of  $f_0 = 2.5$  GHz, and a depression angle of  $\theta_z = 45^\circ$ . The aircraft flies a circular path of radius 7000 m at an altitude of 7000 m from the ground plane. The radar uses a sinc shaped time domain compressed waveform.

## V. Results and Analysis

This chapter presents results and analysis describing the point spread function (PSF) characteristics of a point scatterer. First, key observations characterizing the PSF of a radially displaced scatterer is presented. Then, baseline PSF results for a point target located at the scene center (0,0,0) are demonstrated. Both 2D PSFs and 3D plots of the PSFs for the on-center point target are presented and analyzed. PSF results for radially displaced, off-center point targets, are then presented. Again, both 2D PSFs and 3D plots of the PSF responses are illustrated and analyzed.

### 5.1 PSF Characteristics of an Off-center Target

Table 5.1 depicts key observations characterizing the PSF of an off-center point target. With a radial displacement  $d_r$  of 3000 m from the scene center ( $d_r = 0$  m), the PSF of the point target tends to become an elliptic shape from a circular shape. With an additional displacement of  $d_r = 5000$  m, the ellipticity increases. Therefore, as  $\Delta d_r$  increases, the PSF becomes more elliptic shaped and asymmetric about the  $z$ -axis. A change in the image plane from  $h = 0$  m to  $h = 3$  m, the PSF response changes from a fully focused image to a degraded annulus shaped image. When  $h = 0$  m (i.e. ground plane is the image plane), the PSF is fully focused. As  $\Delta h$  increases, the width of the annulus decreases. This is an indication that a target is present but its image is not focused. Also for  $h > 0$ , the peak PSF response is no longer observed at the true target location. A change in  $\theta_z$ , changes the radius of the annulus. Maximum increase in the annulus radius occurs at  $\theta_z = 45^\circ$ .

### 5.2 PSF Results: Point target at the origin

The PSF of an on-center (0,0,0) point target serves as a basis for characterizing PSF of displaced point targets. Hence, this section provides a detailed analysis of the on-center point target PSF.

First, the 2D PSF of a scatterer in the ground plane is presented. Then, 2D PSFs in different image planes at heights 1, 2, and 3 meters from the ground plane

Table 5.1: Results characterizing PSF of a radially displaced point scatterer. In this table,  $\Delta d_r$  represents changes in the radial displacements of the point target along the positive  $x$ -axis in the scene,  $\Delta h$  represents changes in the locations of the image plane above the ground plane where  $h = 0$  is the ground plane and  $\Delta\theta_z$  represents changes in the depression angle.

Parameters	Observation
$\Delta d_r$ (radial displacement)	PSF changes from a circle to an ellipse and PSF becomes asymmetric about the $z$ -axis as $d_r$ increases.
$\Delta h$ (image plane)	Width of the annulus decreases as $h$ increases. Also for $h > 0$ , the peak PSF response is no longer observed at the true target location.
$\Delta\theta_z$ (depression angle)	Annulus radius changes. Maximum occurs at $\theta_z = 45^\circ$

are presented. Similarly, the 3D plot of the PSF of a scatterer at the ground plane is presented. Then, 3D plots of the PSFs in different image planes at heights 1, 2, and 3 meters from the ground plane are presented.

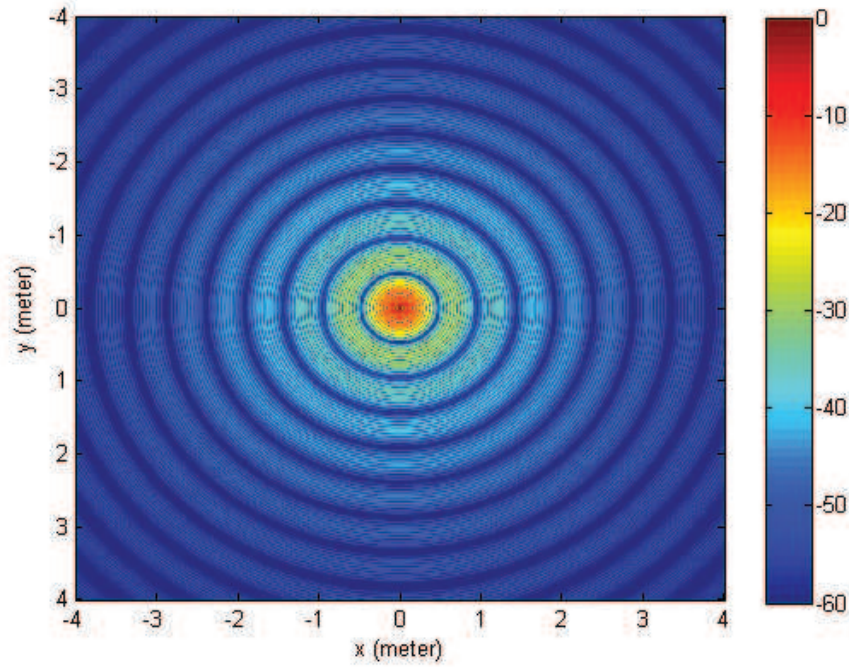


Figure 5.1: 2D PSF for point scatterer located at the scene center (0,0,0). The image was formed for a depression angle  $\theta_z$  of  $45^\circ$ , a bandwidth  $\Delta\omega$  of 0.5 GHz and azimuth span of 0 to  $360^\circ$  [12].

*5.2.1 2D PSF Responses.* Figure 5.1 through Fig. 5.5 show baseline PSF results for a point target located at the origin (0,0,0) or radial displacement  $d_r = 0$  m. Figure 5.1 shows the 2D PSF of a point scatterer located at the scene center using bandwidth  $\Delta\omega$  of 0.5 GHz, and full azimuth coverage of 0 to 360°. The image plane is the ground plane.

Figure 5.2 through Fig. 5.4 show 2D PSFs formed at different heights above the ground plane for a point scatterer located at the scene center (0,0,0). The images were formed for a depression angle of 45° and full azimuth coverage of 0 to 360°. PSF results at height  $h = 1, 2$  and 3 meters are presented in Fig. 5.2 through Fig. 5.4 respectively. As shown, for all focusing heights ( $h$ ) greater than zero (i.e. above the ground plane), the response degrades to an annulus shape. The maximum PSF response within the annulus decreases with  $h$  and are all 20 dB or more below the peak  $h = 0$  ground plane response in Fig. 5.1. The annulus radius is a function of

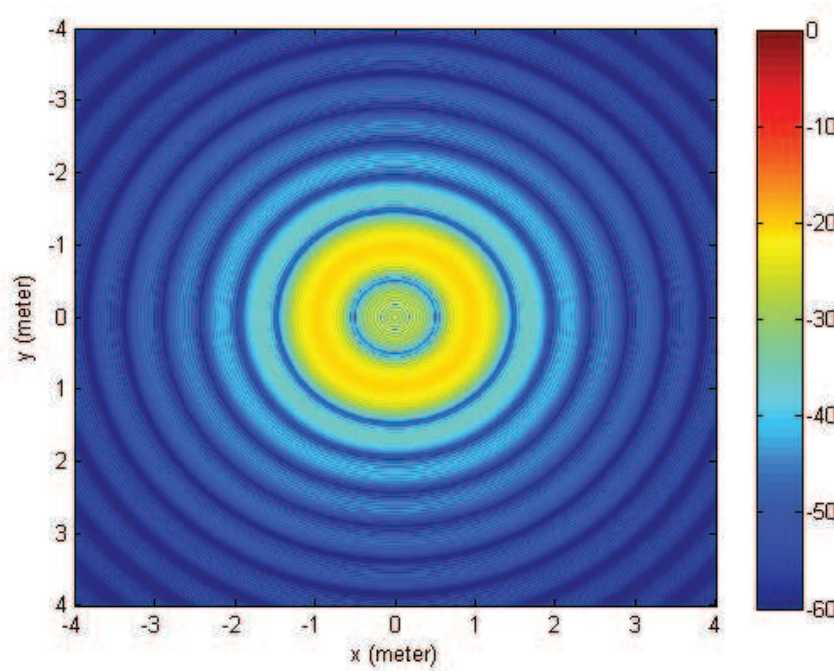


Figure 5.2: 2D PSF for the point scatterer located at the scene center (0,0,0). The image plane is 1 meter above the ground plane. The image was formed for a depression angle  $\theta_z$  of 45°, a bandwidth  $\Delta\omega$  of 0.5 GHz and azimuth span of 0 to 360° [12].

depression angle ( $\theta_z$ ) and height ( $h$ ) above the point target and is given by [12]:

$$r = h \cdot \tan(\theta_z) \quad (5.1)$$

Figure 5.5 shows the  $X$ - $Z$  cut of the 3D PSF results with the point scatterer located at the scene center. This figure illustrates the fact that for an on-center target (i.e. when target's radial displacement  $d_r = 0$ ), the PSF is symmetric about the  $z$ -axis.

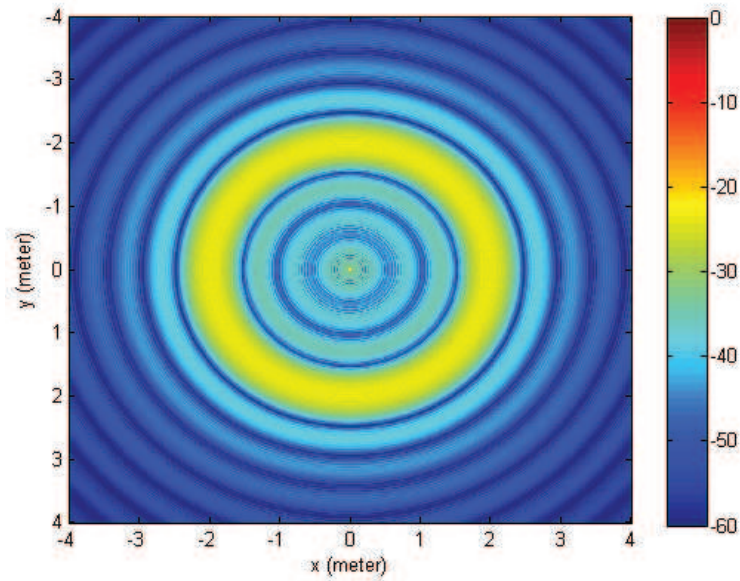


Figure 5.3: 2D PSF for the point scatterer located at the scene center (0,0,0). The image plane is 2 meters above the ground plane. The image was formed for a depression angle  $\theta_z$  of  $45^\circ$ , a bandwidth  $\Delta\omega$  of 0.5 GHz and azimuth span of 0 to  $360^\circ$  [12].



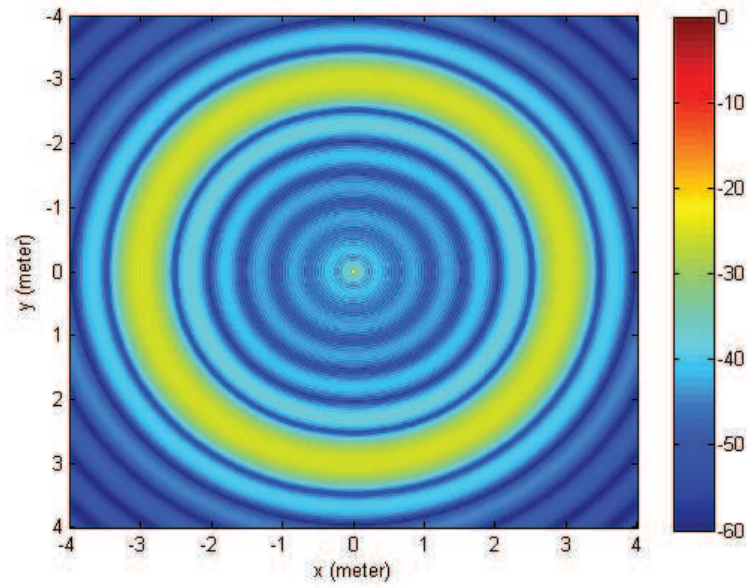


Figure 5.4: 2D PSF for the point scatterer located at the scene center (0,0,0). The image plane is 3 meters above the ground plane. The image was formed for a depression angle  $\theta_z$  of  $45^\circ$ , a bandwidth  $\Delta\omega$  of 0.5 GHz and azimuth span of 0 to  $360^\circ$  [12].

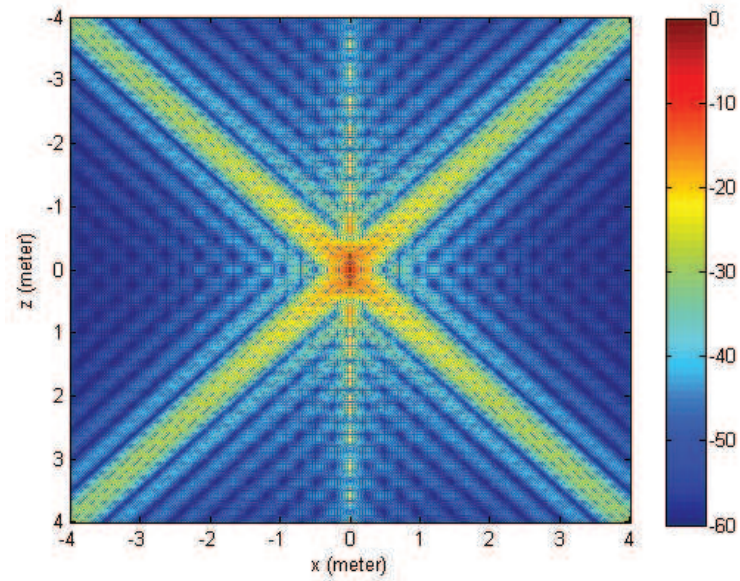


Figure 5.5: X-Z plane cut of the 3D PSF for point scatterer located at the scene center (0,0,0). The image was formed for a depression angle  $\theta_z$  of  $45^\circ$ , a bandwidth  $\Delta\omega$  of 0.5 GHz and azimuth span of 0 to  $360^\circ$  [12].

5.2.2 *3D Plots of the PSF Responses.* Figure 5.6 through Fig. 5.9 show 3D plots of the PSFs formed at different heights above the ground plane for a point scatterer located at the scene center  $(0,0,0)$  or radial displacement  $d_r = 0$  m. The images were formed for a depression angle  $\theta_z$  of  $45^\circ$  and full azimuth coverage of 0 to  $360^\circ$ . PSF results at height  $h = 0, 1, 2$  and 3 meters are presented in Fig. 5.6 through Fig. 5.9 respectively, where  $h = 0$  is the ground plane. As shown, when focusing at heights greater than zero, the response degrades to an annulus shape. Fig. 5.10 shows the 3D PSF results for CSAR conditions with the point scatterer located at the scene center. Consistent with published results [1,13], the 3D PSF is cone shaped and symmetric about the  $z$ -axis. For all  $h$ , the peak PSF response remains at the true target location.

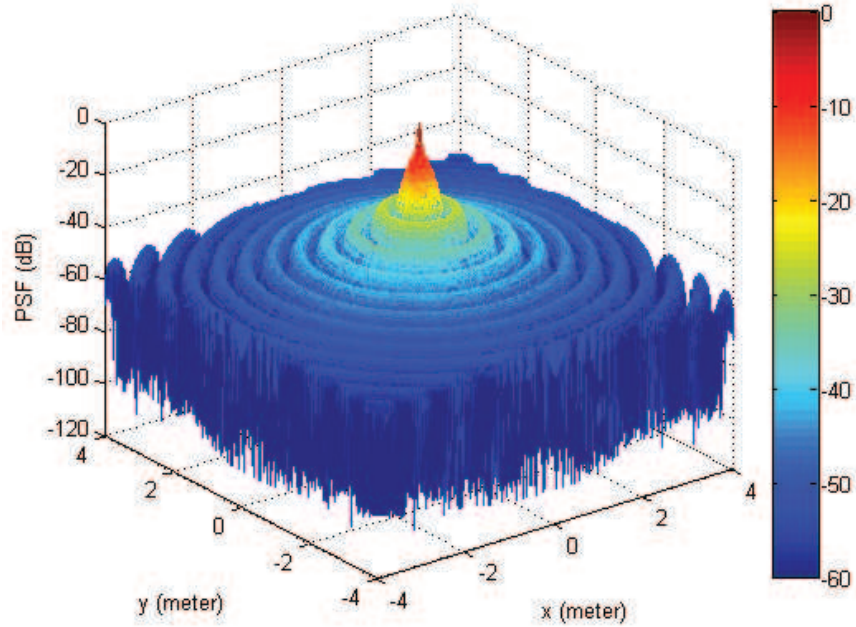


Figure 5.6: 3D plot of PSF for the point scatterer located at the scene center  $(0,0,0)$ . The image plane is the ground plane. The image was formed for a depression angle  $\theta_z$  of  $45^\circ$ , a bandwidth  $\Delta\omega$  of 0.5 GHz and azimuth span of 0 to  $360^\circ$

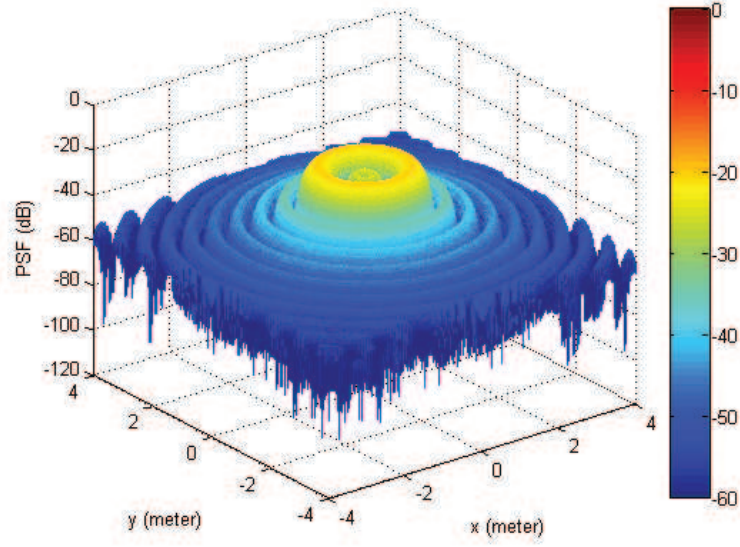


Figure 5.7: 3D plot of PSF for the point scatterer located at the scene center (0,0,0). The image plane is 1 meter above the ground plane. The image was formed for a depression angle  $\theta_z$  of  $45^\circ$ , a bandwidth  $\Delta\omega$  of 0.5 GHz and azimuth span of 0 to  $360^\circ$

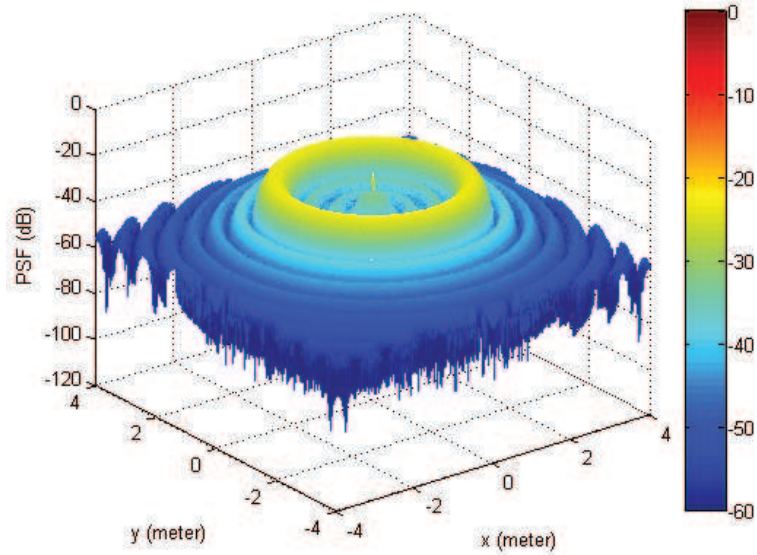


Figure 5.8: 3D plot of PSF for the point scatterer located at the scene center (0,0,0). The image plane is 2 meters above the ground plane. The image was formed for a depression angle  $\theta_z$  of  $45^\circ$ , a bandwidth  $\Delta\omega$  of 0.5 GHz and azimuth span of 0 to  $360^\circ$



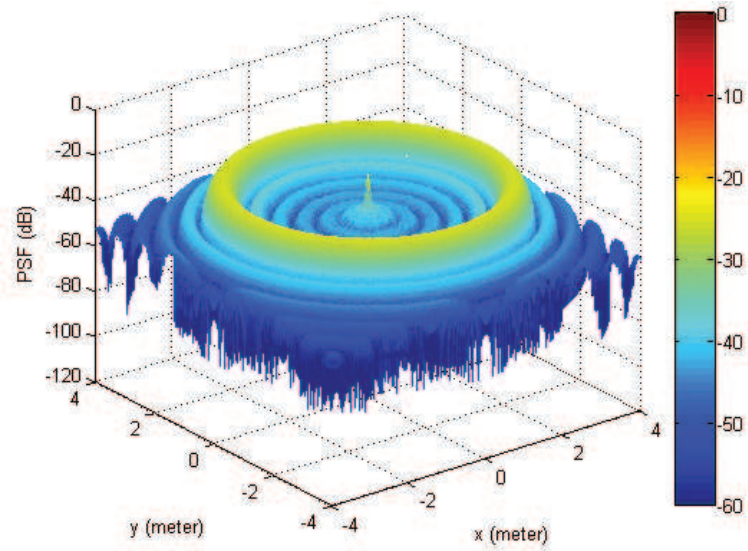


Figure 5.9: 3D plot of PSF for the point scatterer located at the scene center (0,0,0). The image plane is 3 meters above the ground plane. The image was formed for a depression angle  $\theta_z$  of  $45^\circ$ , a bandwidth  $\Delta\omega$  of 0.5 GHz and azimuth span of 0 to  $360^\circ$

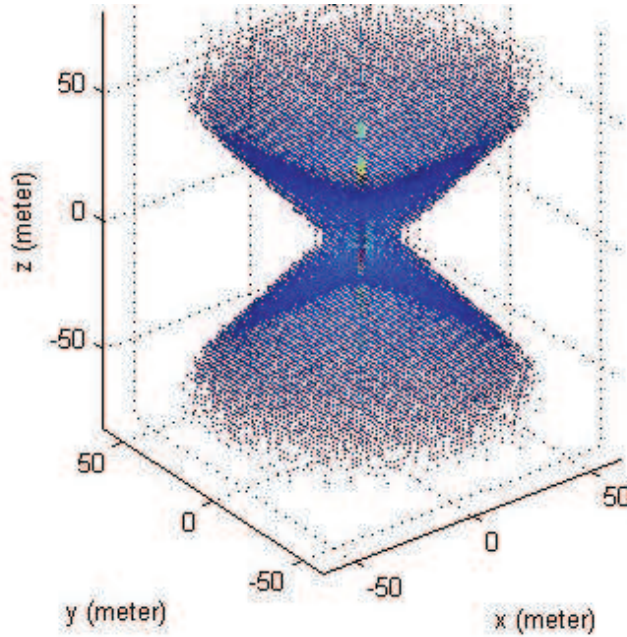


Figure 5.10: 3D PSF for point scatterer located at the scene center (0,0,0). The image was formed for a depression angle  $\theta_z$  of  $45^\circ$ , a bandwidth  $\Delta\omega$  of 0.5 GHz and azimuth span of 0 to  $360^\circ$

### 5.3 PSF Results: Radially displaced point target

As mentioned earlier in Chapter 4, an analytic closed-form solution describing the PSF of a radially displaced target is difficult to obtain [19]. Hence, PSF results presented here for a radially displaced point target is based on computer simulation. First, the 2D PSF of a scatterer at the ground plane (i.e.  $h = 0$  m) is presented. Then, 2D PSFs at different image planes located at heights of 1, 2, and 3 meters above the ground plane are presented. Similarly, the 3D plot of the PSF of a scatterer at the ground plane is presented. Then, 3D plots of PSFs at different image planes located at heights 1, 2, and 3 meters above the ground plane is presented.

*5.3.1 2D PSF Responses.* Figure 5.11 through Fig. 5.14 show 2D PSF results for point target displaced  $d_r = 3000$  meters along the positive  $x$ -axis. Figure 5.11 shows the 2D PSF of a point scatterer using a depression angle  $\theta_z$  of  $45^\circ$ , a bandwidth  $\Delta\omega$  of 0.5 GHz, and full azimuth coverage of 0 to  $360^\circ$ . The image plane is the ground plane.

Fig. 5.12 through Fig. 5.14 show 2D PSFs formed at different heights above the ground plane for a point scatterer displaced 3000 meters along the positive  $x$ -axis. The images were formed for a depression angle of  $\theta_z = 45^\circ$  and full azimuth coverage of 0 to  $360^\circ$ . In these cases, the previous annulus responses become elliptical and asymmetric about the  $z$ -axis. PSF results at height  $h = 1, 2$ , and 3 meters are presented in Fig. 12 through Fig. 14, respectively. For  $h > 0$ , the peak response is no longer observed at the true target location (i.e.  $d_r = 3000$  m). Figure 5.15 shows the  $X$ - $Z$  cut of the 3D PSF results for the point scatterer displaced 3000 meters along the positive  $x$ -axis. In this case, previous cone shown in Fig. 5.10 becomes a tilted cone and thus  $X$ - $Z$  cut is tilted.

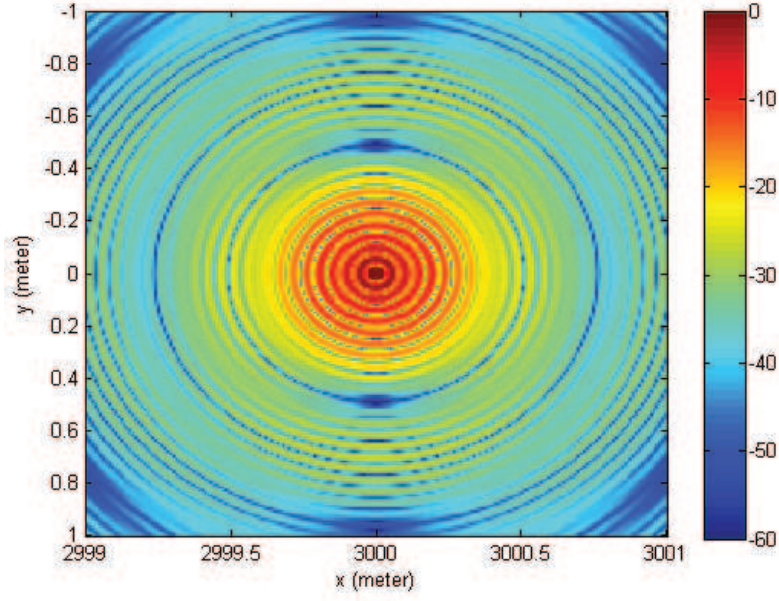


Figure 5.11: 2D PSF for point scatterer displaced 3000 meters along the positive  $x$ -axis. The image plane is the ground plane. The image was formed for a depression angle  $\theta_z$  of  $45^\circ$ , a bandwidth  $\Delta\omega$  of 0.5 GHz and azimuth span of 0 to  $360^\circ$  [12].

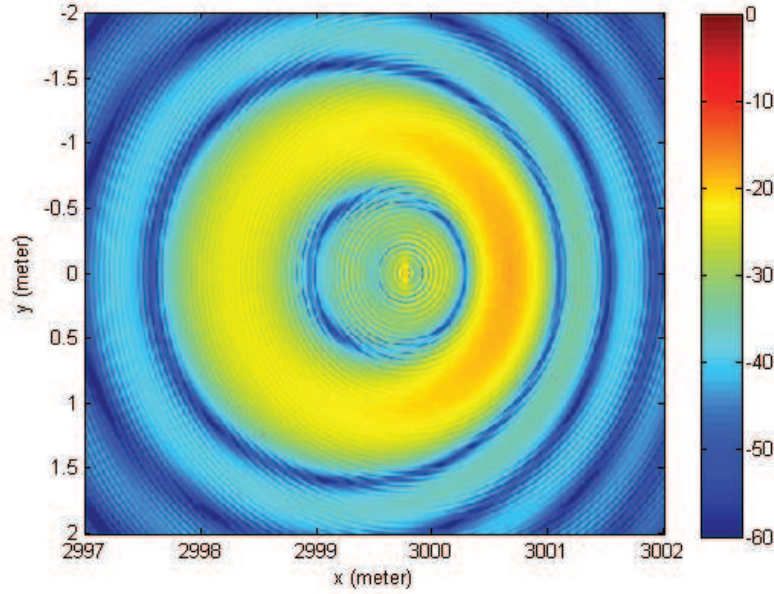


Figure 5.12: 2D PSF for point scatterer displaced 3000 meters along the positive  $x$ -axis. The image plane is 1 meter above the ground plane. The image was formed for a depression angle  $\theta_z$  of  $45^\circ$ , a bandwidth  $\Delta\omega$  of 0.5 GHz and azimuth span of 0 to  $360^\circ$  [12].

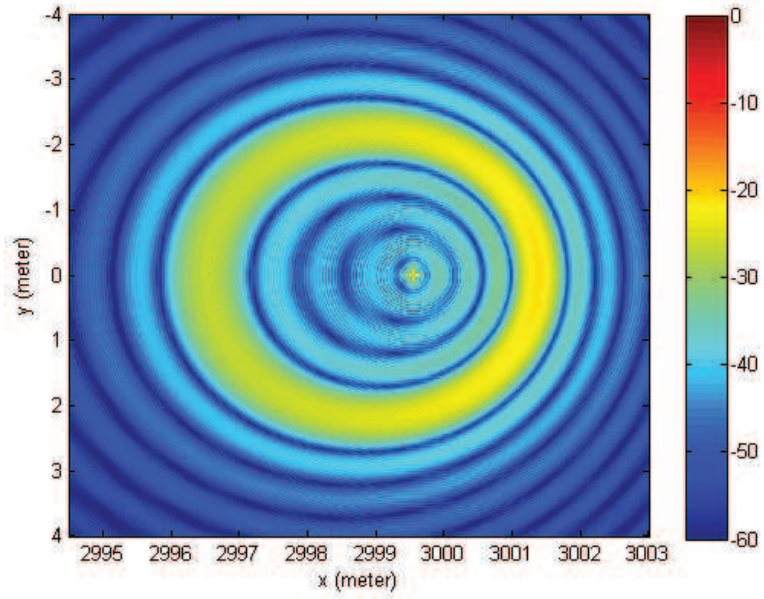


Figure 5.13: 2D PSF for point scatterer displaced 3000 meters along the positive  $x$ -axis. The image plane is 2 meters above the ground plane. The image was formed for a depression angle  $\theta_z$  of  $45^\circ$ , a bandwidth  $\Delta\omega$  of 0.5 GHz and azimuth span of 0 to  $360^\circ$  [12].

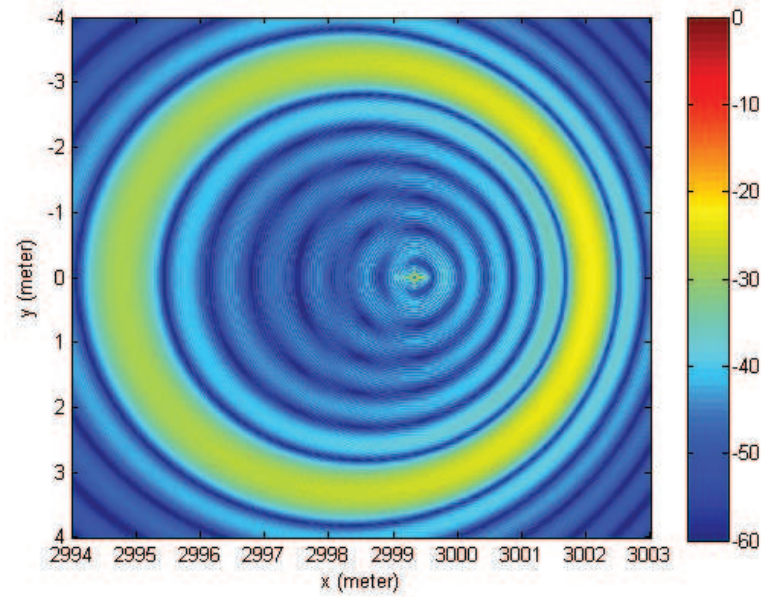


Figure 5.14: 2D PSF for point scatterer displaced 3000 meters along the positive  $x$ -axis. The image plane is 3 meters above the ground plane. The image was formed for a depression angle  $\theta_z$  of  $45^\circ$ , a bandwidth  $\Delta\omega$  of 0.5 GHz and azimuth span of 0 to  $360^\circ$  [12].



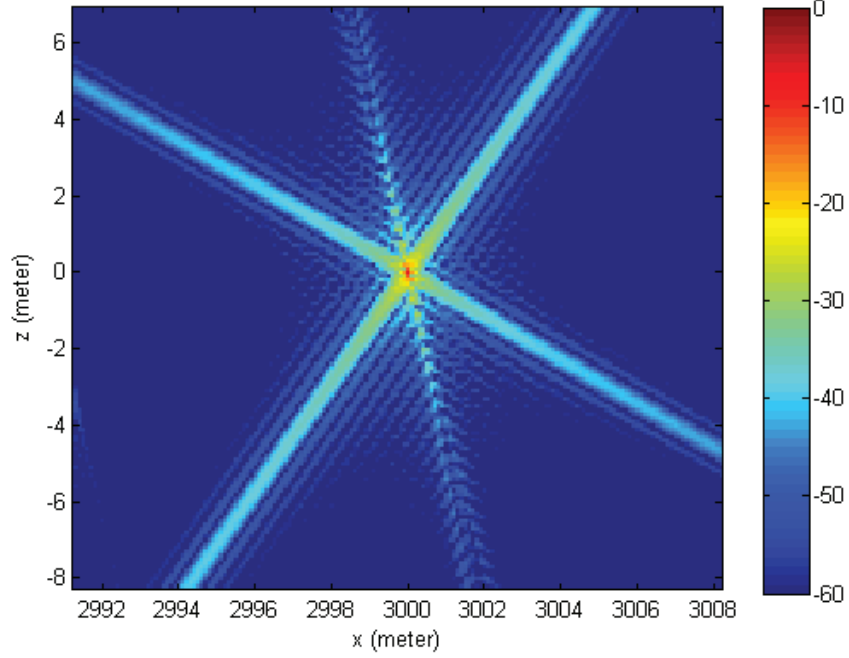


Figure 5.15:  $X$ - $Z$  plane cut of the 3D PSF for point scatterer displaced 3000 meters along the positive  $x$ -axis. The image was formed for a depression angle  $\theta_z$  of  $45^\circ$ , a bandwidth  $\Delta\omega$  of 0.5 GHz and azimuth span of 0 to  $360^\circ$  [12].

Figure 5.16 through Fig. 5.19 show 2D PSF results for point target displaced  $d_r = 5000$  m along the positive  $x$ -axis. The images were formed for a depression angle  $\theta_z$  of  $45^\circ$ , full azimuth coverage of 0 to  $360^\circ$  and at height  $h = 0, 1, 2$  and 3 meters respectively from the ground plane. With the additional radial displacement, the PSF tends to become more elliptically shaped. For  $h > 0$ , PSF responses degrade to annulus shapes and asymmetric about the  $z$ -axis. Also for  $h > 0$ , the peak PSF response is no longer observed at the true target location (i.e.  $d_r = 5000$  m).

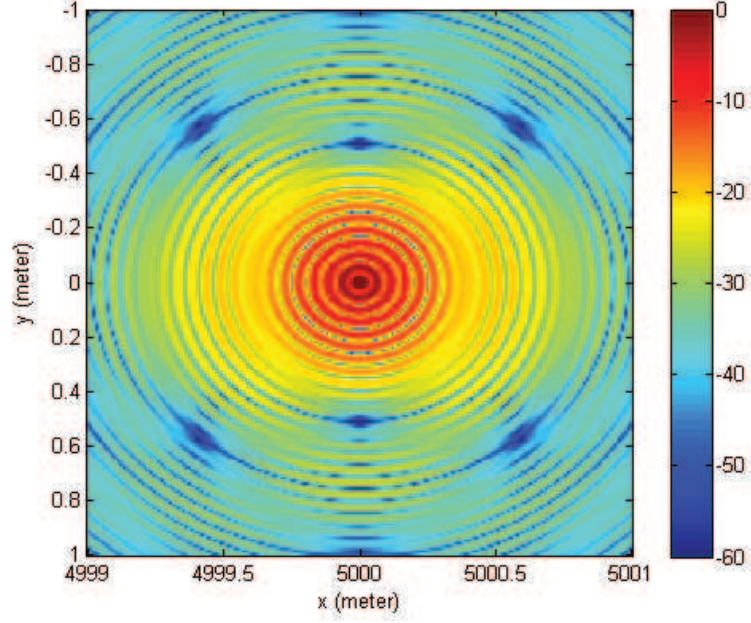


Figure 5.16: 2D PSF for point scatterer displaced 5000 meters along the positive  $x$ -axis. The image plane is the ground plane. The image was formed for a depression angle  $\theta_z$  of  $45^\circ$ , a bandwidth  $\Delta\omega$  of 0.5 GHz and azimuth span of 0 to  $360^\circ$

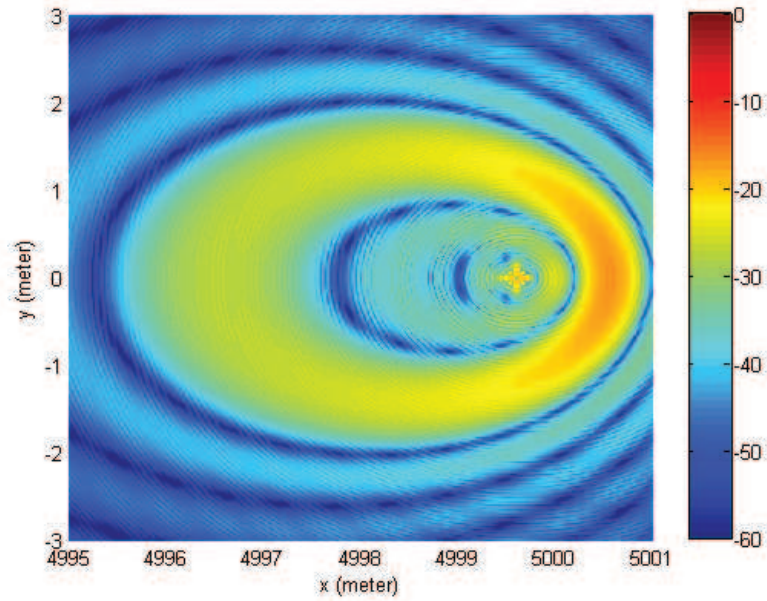


Figure 5.17: 2D PSF for point scatterer displaced 5000 meters along the positive  $x$ -axis. The image plane is 1 meter above the ground plane. The image was formed for a depression angle  $\theta_z$  of  $45^\circ$ , a bandwidth  $\Delta\omega$  of 0.5 GHz and azimuth span of 0 to  $360^\circ$

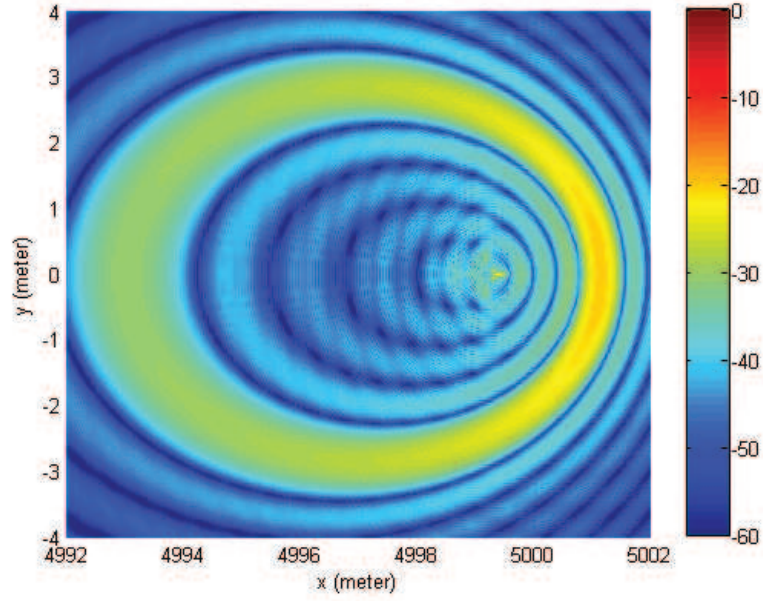


Figure 5.18: 2D PSF for point scatterer displaced 5000 meters along the positive  $x$ -axis. The image plane is 2 meters above the ground plane. The image was formed for a depression angle  $\theta_z$  of  $45^\circ$ , a bandwidth  $\Delta\omega$  of 0.5 GHz and azimuth span of 0 to  $360^\circ$

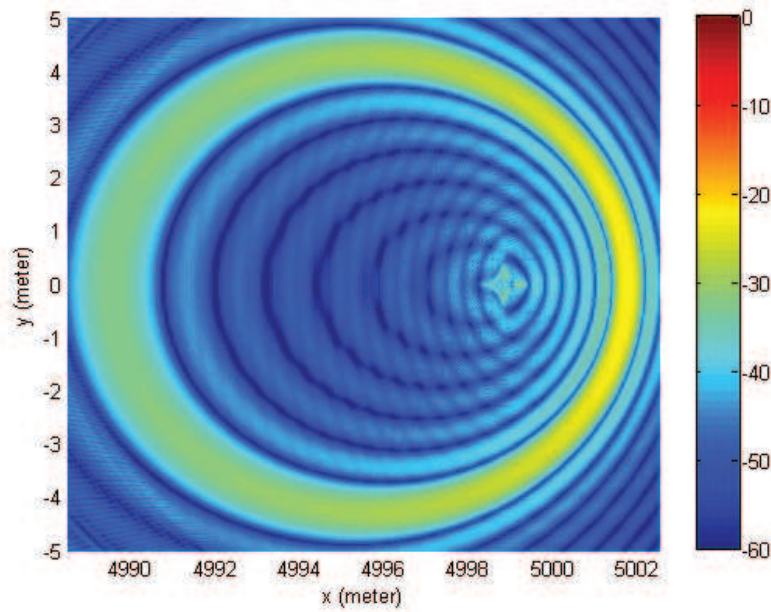


Figure 5.19: 2D PSF for point scatterer displaced 5000 meters along the positive  $x$ -axis. The image plane is 3 meters above the ground plane. The image was formed for a depression angle  $\theta_z$  of  $45^\circ$ , a bandwidth  $\Delta\omega$  of 0.5 GHz and azimuth span of 0 to  $360^\circ$

*5.3.2 3D plots of the PSF Responses.* Figure 5.20 through Fig. 5.23 show 3D plots of PSFs formed at different heights above the ground plane for a point scatterer displaced  $d_r = 3000$  meters along the positive  $x$ -axis. The images were formed for a depression angle  $\theta_z$  of  $45^\circ$  and full azimuth coverage of 0 to  $360^\circ$ . PSF results at height  $h = 0, 1, 2$  and 3 meters are presented in Fig. 5.20 through Fig. 5.23, respectively, where  $h = 0$  is the ground plane. As shown, when focusing heights are greater than zero (i.e. image plane is above the ground plane), the previous annulus responses become elliptically shaped and asymmetric about the  $z$ -axis. Also for  $h > 0$ , 3D plots of the PSF responses become tilted.

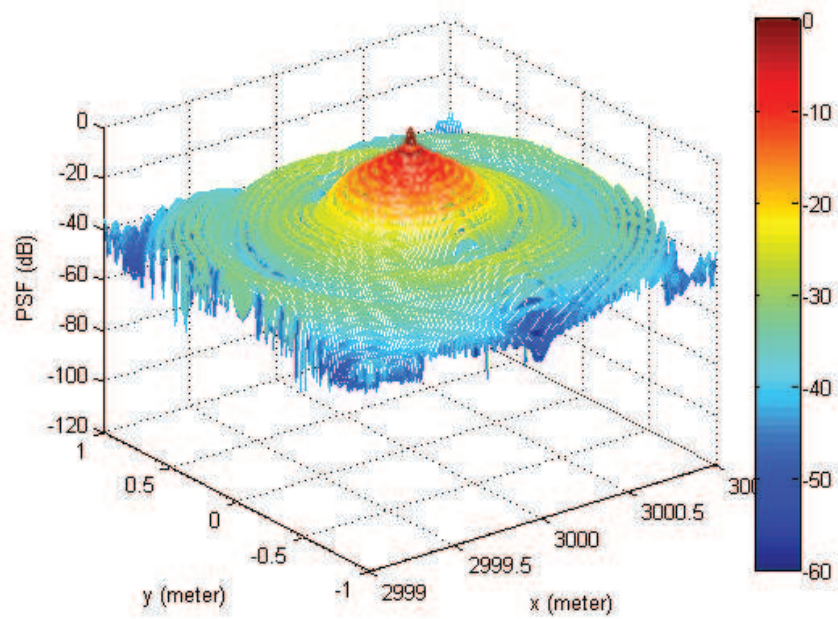


Figure 5.20: 3D plot of PSF for the point scatterer displaced 3000 meters along the positive  $x$ -axis. The image plane is the ground plane. The image was formed for a depression angle  $\theta_z$  of  $45^\circ$ , a bandwidth  $\Delta\omega$  of 0.5 GHz and azimuth span of 0 to  $360^\circ$



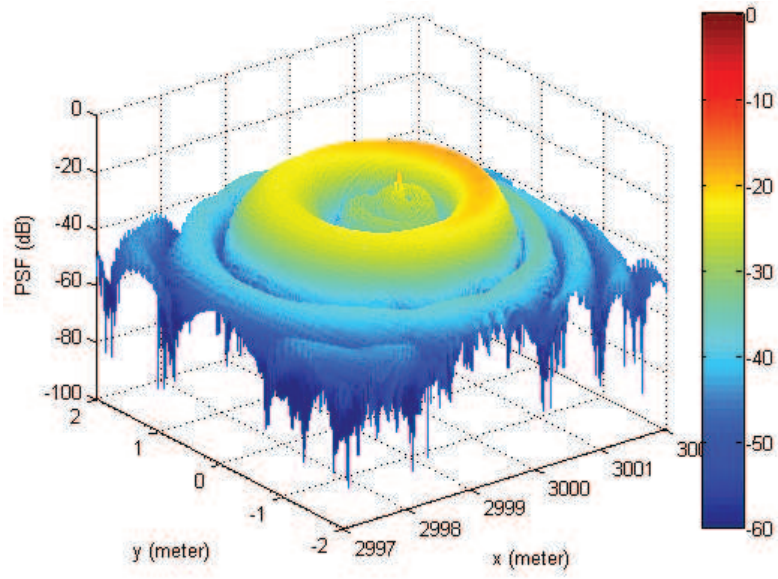


Figure 5.21: 3D plot of PSF for the point scatterer displaced 3000 meters along the positive  $x$ -axis. The image plane is 1 meter above the ground plane. The image was formed for a depression angle  $\theta_z$  of  $45^\circ$ , a bandwidth  $\Delta\omega$  of 0.5 GHz and azimuth span of 0 to  $360^\circ$

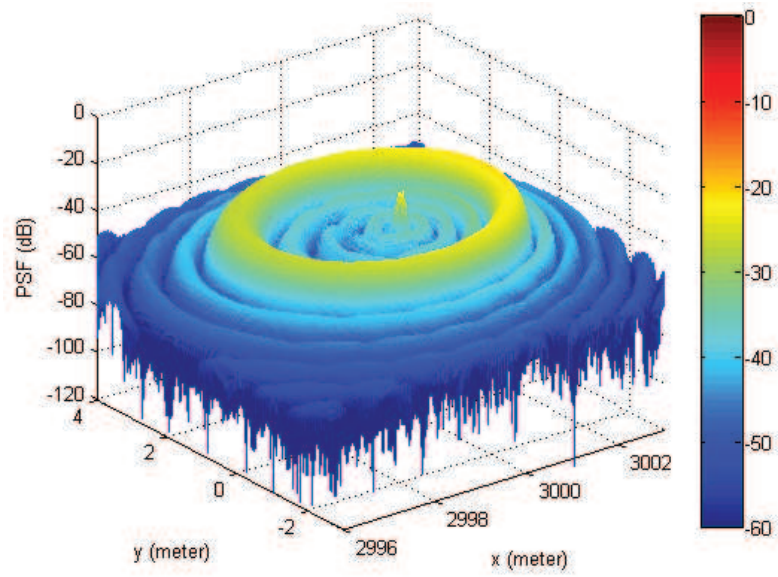


Figure 5.22: 3D plot of PSF for the point scatterer displaced 3000 meters along the positive  $x$ -axis. The image plane is 2 meters above the ground plane. The image was formed for a depression angle  $\theta_z$  of  $45^\circ$ , a bandwidth  $\Delta\omega$  of 0.5 GHz and azimuth span of 0 to  $360^\circ$

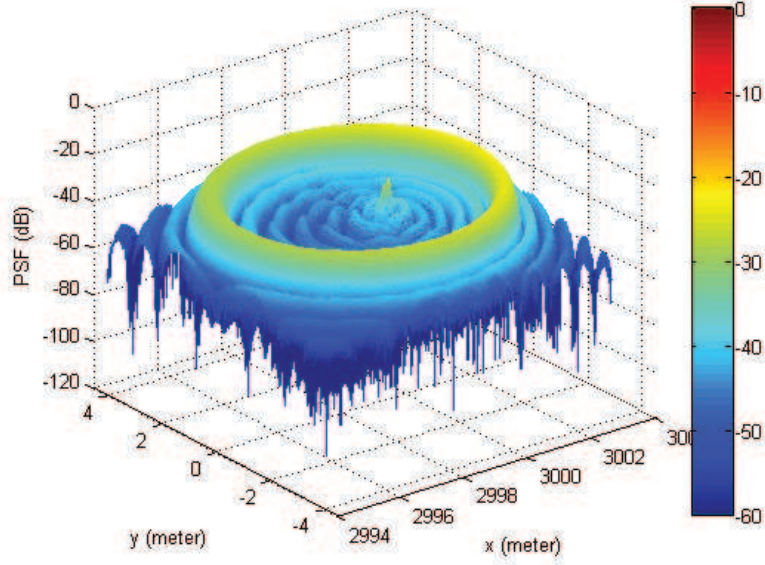


Figure 5.23: 3D plot of PSF for the point scatterer displaced 3000 meters along the positive  $x$ -axis. The image plane is 3 meters above the ground plane. The image was formed for a depression angle  $\theta_z$  of  $45^\circ$ , a bandwidth  $\Delta\omega$  of 0.5 GHz and azimuth span of 0 to  $360^\circ$

Figure 5.24 through Fig. 5.27 show 3D plots of PSFs formed at different heights above the ground plane for a point scatterer displaced  $d_r = 5000$  meters along the positive  $x$ -axis. The images were formed for a depression angle of  $\theta_z = 45^\circ$  and full azimuth coverage of 0 to  $360^\circ$ . 3D PSF results at height  $h = 0, 1, 2$  and 3 meters are presented in Fig. 5.24 through Fig. 5.27 respectively, where  $h = 0$  is the ground plane. With the additional radial displacement, the PSF ellipticity increases relative to previous cases and asymmetric about the  $z$ -axis. 3D plot of the PSF response becomes more tilted.

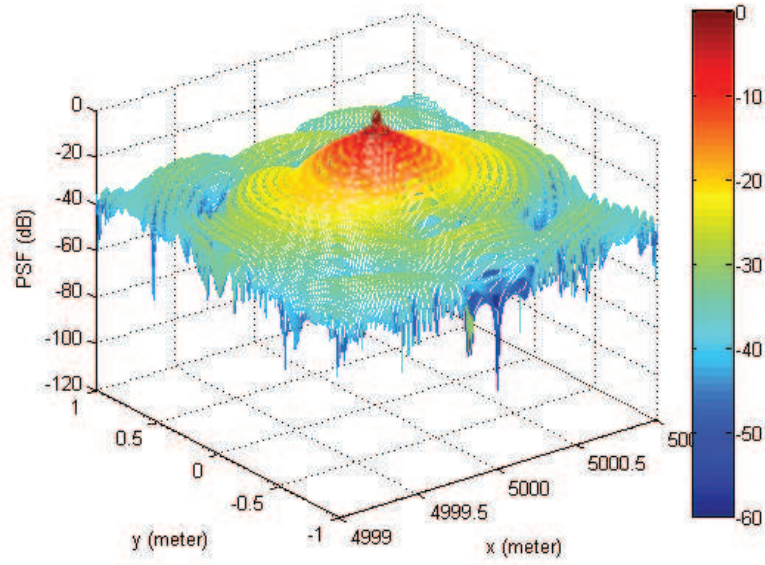


Figure 5.24: 3D plot of PSF for the point scatterer displaced 5000 meters along the positive  $x$ -axis. The image plane is the ground plane. The image was formed for a depression angle  $\theta_z$  of  $45^\circ$ , a bandwidth  $\Delta\omega$  of 0.5 GHz and azimuth span of 0 to  $360^\circ$

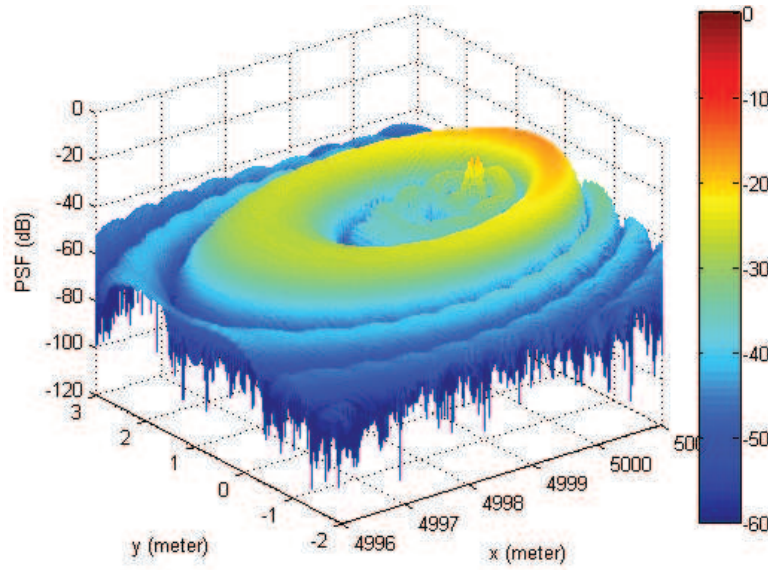


Figure 5.25: 3D plot of PSF for the point scatterer displaced 5000 meters along the positive  $x$ -axis. The image plane is 1 meter above the ground plane. The image was formed for a depression angle  $\theta_z$  of  $45^\circ$ , a bandwidth  $\Delta\omega$  of 0.5 GHz and azimuth span of 0 to  $360^\circ$

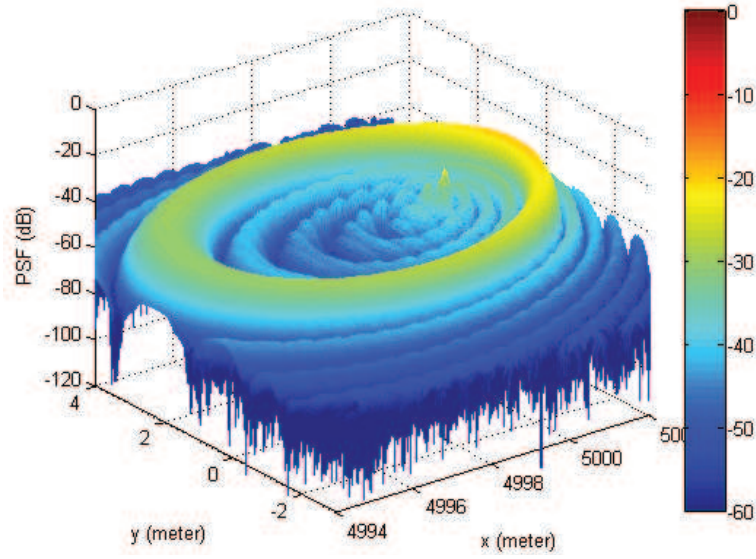


Figure 5.26: 3D plot of PSF for the point scatterer displaced 5000 meters along the positive  $x$ -axis. The image plane is 2 meters above the ground plane. The image was formed for a depression angle  $\theta_z$  of  $45^\circ$ , a bandwidth  $\Delta\omega$  of 0.5 GHz and azimuth span of 0 to  $360^\circ$

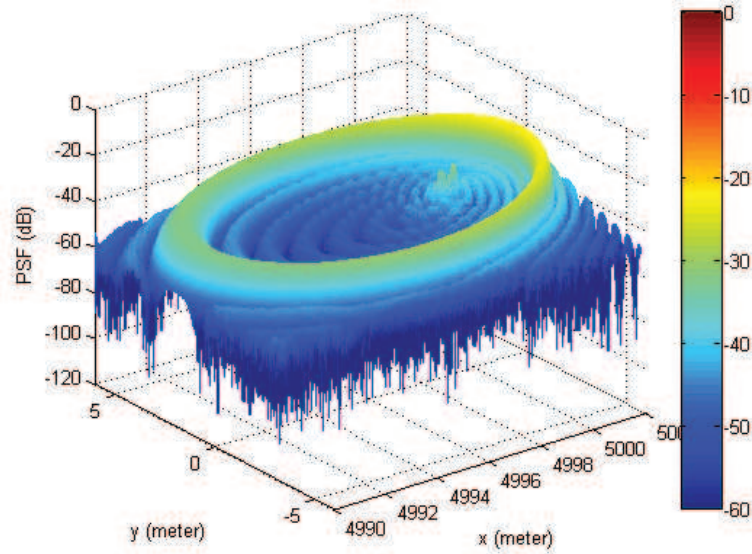


Figure 5.27: 3D plot of the PSF for the point scatterer displaced 5000 meters along the positive  $x$ -axis. The image plane is 3 meters above the ground plane. The image was formed for a depression angle  $\theta_z$  of  $45^\circ$ , a bandwidth  $\Delta\omega$  of 0.5 GHz and azimuth span of 0 to  $360^\circ$

#### 5.4 Summary

This chapter provides results describing the PSF characteristics of a point scatterer. The PSFs were formed for a depression angle  $\theta_z$  of  $45^\circ$ , a bandwidth  $\Delta\omega$  of 0.5 GHz and azimuth span of 0 to  $360^\circ$ . Both 2D PSFs and 3D plots of the PSFs are presented for a point target located at the scene center (0,0,0) or radial displacement  $d_r = 0$  m. Then, 2D PSFs and 3D plot of the PSFs for the radially displaced ( $d_r = 3000, 5000$  m) point target have been presented. Results show that for an on-center ( $d_r = 0$  m) point target, the 2D PSF is focused and circular. The 3D PSF response is cone shaped and symmetric about the  $z$ -axis. This result is consistent with previously published research [1, 13].

For a radially displaced point scatterer, the PSF becomes elliptic. As radial displacement  $d_r$  increases from 3000 m to 5000 m, the PSF becomes more elliptic shaped and asymmetric about the  $z$ -axis. A change in the image plane from  $h = 0$  m to  $h = 3$  m, the PSF response changes from a fully focused image to a degraded annulus shaped image. Also for  $h > 0$ , the peak PSF response is no longer observed at the true target location. A change in the depression angle  $\theta_z$ , changes the annulus radius. The maximum increase in the annulus radius occurs when  $\theta_z = 45^\circ$ .



## VI. Conclusions

The Point Spread Function (PSF) of a radially displaced point scatterer is characterized for CSAR imagery via simulation. Backprojection image formation was used to simulate the PSF of the on-center and off-center point targets. Important radar parameters used for this research include a radar center frequency  $f_0$  of 2.5 GHz, range resolution  $\Delta_r$  of 0.3 m and depression angle  $\theta_z$  of  $45^\circ$ . Contribution of this research to SAR application has been introduced. Finally, future research on this topic has been presented.

### 6.1 Research Summary

Simulated 2D and 3D PSF results are presented for a point scatterer using Circular Synthetic Aperture Radar (CSAR) processing. When the scatterer is located at the imaging scene center, with full  $360^\circ$  azimuth coverage and a depression angle  $\theta_z$  of  $45^\circ$  the scattering response is circular and symmetrical around the  $z$ -axis. The 3D PSF response is cone shaped [1, 11, 13].

When the point target is radially displaced, the PSF response is elliptic and no longer symmetric about the  $z$ -axis. In this case, the previous 3D cone becomes more tilted as the distance from the scene center increases. Thus, a 2D elevation slice of the tilted cone gives a conic section. For the cases simulated, the conic section was an ellipse having increased ellipticity with larger radial displacement.

Another PSF characteristic was observed by forming 2D PSF responses at heights of  $h = 1, 2$  and 3 meters above the ground plane. It was observed that the maximum PSF response within the annulus decreases with  $h$ . For example, the peak response at  $h = 1$  was 20 dB or more below the peak ground plane response at  $h = 0$ . As a result, the annulus responses appeared wider at the lower heights. For the point scatterers displaced from the scene center, a 2D cut at a height above the ground plane illustrates the combined effect of the elliptical shape and annulus broadening as depicted in Figure 5.17. Also for the radially displaced scatterer when  $h > 0$ , the peak PSF response is no longer observed at the true target location. It was

also observed that a change in the depression angle  $\theta_z$ , changes the annulus radius. The maximum increase in the annulus radius occurs at  $\theta_z$  of  $45^\circ$ ,

## 6.2 *Contribution to SAR research*

As discussed in the introduction, there is an important need to image large scene sizes with CSAR. Unfortunately, as a result of the imaging geometry, the PSF is not invariant to scatterer position in the scene. In order to perform image interpretation or exploitation of large scenes using CSAR, it is important to understand how the PSF changes as a function of the target's position in the scene. This research provides one experimental step toward obtaining this understanding.

In addition, this research provides insight into how one might formulate an analytic solution to the problem. Further, since many signal and image processing approaches to detection and ATR rely on knowledge of the system PSF, results of this thesis could lead to new and improved algorithms for CSAR imaging of large scenes. In particular, the development of target recognition and detection approaches for both stationary (e.g. SAR) and moving targets (e.g., GMTI) could benefit from this research.

## 6.3 *Future Research on Radially Displaced Targets in CSAR*

As stated earlier, this research endeavor characterized the PSF of a radially displaced target in CSAR imagery. The following section highlights potential follow-on research to build on the fundamentals of this thesis topic.

*6.3.1 CSAR response to canonical shapes.* One direction of research could be to investigate the image response of some canonical shapes at radially displaced locations. Canonical shapes such as dihedrals, trihedrals, cylinders would be interesting and important shapes to consider. Understanding these responses would be an important step towards understanding the images of complex targets such as the buildings, motor vehicles, etc. leading to many persistent staring radar applications..

### 6.3.2 *Analytic PSF expression for radially displaced point scatterers.*      Re-

search has been conducted to find an analytic closed-form solution describing the PSF of a point target centered at origin [13]. This solution involves a formulation that includes Bessel function evaluation. For a radially displaced point target, an analytical closed-form solution has not yet been developed. One approach towards developing an analytical solution could involve transforming the on-center [13] analytical solution based on insight provided in this thesis research. Another avenue of investigation could include the development of a numerical approximation that describes the PSF of a radially displaced target.

### 6.3.3 *Detection and ATR algorithms based on PSF response.*      Many signal

processing algorithms take advantage of a priori PSF knowledge. Algorithms using this PSF knowledge may be a fruitful area of research.



## Bibliography

1. Aleksoff, C. “3-D ISAR Enhanced Opto-Electric Processing”. *Proceedings of SPIE Symposium on Defense and Security: In Radar Processing, Technology, and Applications*, volume 2845, 196–204. The International Society for Optical Engineering (SPIE), Orlando, FL, November 1996.
2. Bauck, J. L. and W. K. Jenkins. “Convolution-Backprojection Image Reconstruction for Bistatic Synthetic Aperture Radar”. *Proceedings of International Symposium on Circuits and Systems*, volume 3. Institute of Electrical and Electronics Engineers (IEEE), May 1989.
3. Bryant, M., L. Gostin, and M. Soumekh. “3-D E-CSAR Imaging of a T-72 Tank and Synthesis of its SAR Reconstructions”. *IEEE Transactions on Aerospace and Electronic Systems*, 39(1), January 2003.
4. Carrara, Walter G., Ron S. Goodman, and Ronald M. Majewaski. *Spotlight Synthetic Aperture Radar Signal Processing Algorithms*. Artech House, Inc., Norwood, MA, 1995.
5. Desai, Mita D. and W. Kenneth Jenkins. “Convolution Backprojection Image Reconstruction for Spotlight Mode Synthetic Aperture Radar”. *IEEE Transactions on Image Processing*, 1(4), October 1992.
6. Ding, Yu and Jr. David C. Munson. “A Fast Back-Projection Algorithm for Bistatic SAR Imaging”. *Proceedings of International Conference on Image Processing*, volume 2. Institute of Electrical and Electronics Engineers (IEEE), September 2002.
7. Ishimaru, A., T. Chan, and Y. Kuga. “An Imaging Technique Using Confocal Synthetic Aperture Radar”. *IEEE Transactions on Geoscience and Remote Sensing*, 36(5), 1998.
8. Jain, Anil K. *Fundamentals of Digital Image Processing*. Prentice Hall, New Jersey, NJ, 1989.
9. Jakowatz, Charles V., Daniel E. Wahl, Paul H. Eichel, Dennis C. Ghiglia, and Paul A. Thompson. *Spotlight-Mode Synthetic Aperture Radar: A Signal Processing Approach*. Kluwer Academic Publishers, 101 Philip Drive, Assinippi Park, Norwell, MA 02061, 1996.
10. Mahafza, Bassem R. *Radar Systems Analysis and Design Using Matlab*. Chapman & Hall/CRC, 2000. ISBN: 1584881828.
11. Majumder, Uttam K., Michael A. Temple, Michael J. Minardi, and Edmund G. Zelnio. “3D Point Spread Function Characterization of a Radially Displaced Scatterer Using Circular Synthetic Aperture Radar”. *In Proceedings of SPIE*

*Symposium on Defense and Security: Algorithms for Synthetic Aperture Radar.* The International Society for Optical Engineering (SPIE), Orlando, FL, April 2007. Accepted for Presentation and Publication.

12. Majumder, Uttam K., Michael A. Temple, Michael J. Minardi, and Edmund G. Zelnio. "Point Spread Function Characterization of a Radially Displaced Scatterer Using Circular Synthetic Aperture Radar". *Proceedings of IEEE Radar Conference*. Institute of Electrical and Electronics Engineers (IEEE), Boston, MA, April 2007. Accepted for Presentation and Publication.
13. Moore, Linda J. *Three-Dimensional Resolution for Circular Synthetic Aperture Radar*. Master's thesis, Graduate School of The Ohio State University, Columbus, Ohio, 2006.
14. Richards, Mark A. *Fundamentals of Radar Signal Processing*. McGraw-Hill, Inc., 1221 Avenue of the Americas, New York, NY 10020, 2005. ISBN: 0071444742.
15. SAIC Champaign, IL. "Xpatch User Manual". User Manual, February 2005.
16. Sandia. "What is Synthetic Aperture Radar". Internet Source, February 2006. Sandia URL- <http://www.sandia.gov/RADAR/whatis.html>.
17. Skolnik, Merrill I. *Introduction to Radar Systems*. McGraw-Hill, Inc., 1221 Avenue of the Americas, New York, NY 10020, third edition, 2001. ISBN: 0072909803.
18. Soumekh, M. "Reconnaissance with Slant Plane Circular SAR Imaging". *IEEE Transactions on Image Processing*, 5(8), August 1996.
19. Soumekh, Mehrdad. *Synthetic Aperture Radar Signal Processing*. John Wiley & Sons, Inc., New York, NY, second edition, 1999.
20. Ulander, Lars M.H., Hans Hellsten, and Gunnar. "Synthetic-Aperture Radar Processing Using Fast Factorized Back-Projection". *IEEE Transactions on Aerospace and Electronic Systems*, 39(3), July 2003.
21. Wiora, Georg. "Radar Signal Processing". Internet Source, October 2005. Wikipedia URL- <http://en.wikipedia.org/wiki/Image:SonarPrincipleEN.svg>.
22. Zeng, Gengsheng L. and Grant T. Gullberg. "Can the Backprojection Filtering Algorithm be as Accurate as the Filtered Backprojection Algorithm?" *Proceedings of Nuclear Science Symposium and Medical Imaging Conference*, volume 3. Institute of Electrical and Electronics Engineers (IEEE), October 1994.

REPORT DOCUMENTATION PAGE					Form Approved OMB No. 0704-0188	
<p>The public reporting burden for this collection of information is estimated to average 1 hour per response, including the time for reviewing instructions, searching existing data sources, gathering and maintaining the data needed, and completing and reviewing the collection of information. Send comments regarding this burden estimate or any other aspect of this collection of information, including suggestions for reducing this burden to Department of Defense, Washington Headquarters Services, Directorate for Information Operations and Reports (0704-0188), 1215 Jefferson Davis Highway, Suite 1204, Arlington, VA 22202-4302. Respondents should be aware that notwithstanding any other provision of law, no person shall be subject to any penalty for failing to comply with a collection of information if it does not display a currently valid OMB control number. <b>PLEASE DO NOT RETURN YOUR FORM TO THE ABOVE ADDRESS.</b></p>						
1. REPORT DATE (DD-MM-YYYY)		2. REPORT TYPE		3. DATES COVERED (From — To)		
22-03-2007		Master's Thesis		October 2006 — March 2007		
4. TITLE AND SUBTITLE  Point Spread Function Characterization of a Radially Displaced Scatterer Using Circular Synthetic Aperture Radar				5a. CONTRACT NUMBER		
				5b. GRANT NUMBER		
				5c. PROGRAM ELEMENT NUMBER		
				5d. PROJECT NUMBER		
6. AUTHOR(S)  Uttam K. Majumder				5e. TASK NUMBER		
				5f. WORK UNIT NUMBER		
7. PERFORMING ORGANIZATION NAME(S) AND ADDRESS(ES) Air Force Institute of Technology Graduate School of Engineering and Management 2950 Hobson Way WPAFB OH 45433-7765				8. PERFORMING ORGANIZATION REPORT NUMBER  AFIT/GE/ENG/07-26		
9. SPONSORING / MONITORING AGENCY NAME(S) AND ADDRESS(ES) Dr. Michael J. Minardi AFRL/SNAS BLDG620 2241 Avionics Circle, WPAFB OH 45433 (937)904-9043 Email: michael.minardi@wpafb.af.mil				10. SPONSOR/MONITOR'S ACRONYM(S) AFRL/SNAS		
				11. SPONSOR/MONITOR'S REPORT NUMBER(S)		
12. DISTRIBUTION / AVAILABILITY STATEMENT  APPROVED FOR PUBLIC RELEASE; DISTRIBUTION UNLIMITED						
13. SUPPLEMENTARY NOTES						
14. ABSTRACT  This research effort investigated characterizing the point spread function (PSF) behavior of radially displaced point scatterers using circular synthetic aperture radar (CSAR). Thus far, research has been conducted to understand PSF of a scatterer located at the imaging scene center. An analytic closed-form solution has been derived assuming the scatterer is located at the origin of the CSAR imaging geometry. However, it is difficult to derive an analytic PSF solution for a scatterer that is radially displaced from the imaging scene center. Using the backprojection image formation algorithm, PSF responses are generated at various point target locations. Consistent with previous studies, the three dimensional PSF for a point target located at the image center is cone shaped and serves as the basis for comparing and characterizing the PSFs of radially displaced scatterers. Simulated results show the impulse response of a radially displaced point scatterer is asymmetric and tends to exhibit increased ellipticity as it moves further from the scene center.						
15. SUBJECT TERMS  Synthetic Aperture Radar, Automatic Target Recognition, Point Spread Function						
16. SECURITY CLASSIFICATION OF:			17. LIMITATION OF ABSTRACT	18. NUMBER OF PAGES	19a. NAME OF RESPONSIBLE PERSON	
a. REPORT	b. ABSTRACT	c. THIS PAGE			Dr. Michael A. Temple	
U	U	U	UU	74	19b. TELEPHONE NUMBER (include area code) (937) 255-3636, ext 4279	